



Bright vigorous winds as signposts of supermassive black hole birth

Davide Fiacconi¹ and Elena M. Rossi²

¹*Center for Theoretical Astrophysics and Cosmology, Institute for Computational Science, University of Zurich, Winterthurerstrasse 190, CH-8057 Zürich, Switzerland*

²*Leiden Observatory, Leiden University, PO Box 9513, NL-2300RA Leiden, the Netherlands*

Accepted 2015 September 24. Received 2015 September 18; in original form 2015 August 7

ABSTRACT

The formation of supermassive black holes is still an outstanding question. In the *quasi-star* scenario, black hole seeds experience an initial super-Eddington growth, that in less than a million years may leave a 10^4 – $10^5 M_{\odot}$ black hole at the centre of a protogalaxy at $z \sim 20$ – 10 . Super-Eddington accretion, however, may be accompanied by vigorous mass-loss that can limit the amount of mass that reaches the black hole. In this paper, we critically assess the impact of radiative driven winds, launched from the surface of the massive envelopes from which the black hole accretes. Solving the full wind equations coupled with the hydrostatic structure of the envelope, we find mass outflows with rates between a few tens and $10^4 M_{\odot} \text{ yr}^{-1}$, mainly powered by advection luminosity within the outflow. We therefore confirm the claim by Dotan et al. that mass losses can severely affect the black hole seed early growth within a quasi-star. In particular, seeds with mass $>10^4 M_{\odot}$ can only form within mass reservoirs $\gtrsim 10^7 M_{\odot}$, unless they are refilled at huge rates ($\gtrsim 100 M_{\odot} \text{ yr}^{-1}$). This may imply that only very massive haloes ($>10^9 M_{\odot}$) at those redshifts can harbour massive seeds. Contrary to previous claims, these winds are expected to be relatively bright (10^{44} – $10^{47} \text{ erg s}^{-1}$), blue ($T_{\text{eff}} \sim 8000 \text{ K}$) objects, that while eluding the *Hubble Space Telescope*, could be observed by the James Webb Space Telescope.

Key words: hydrodynamics – radiation: dynamics – methods: analytical – stars: massive – stars: winds, outflows.

1 INTRODUCTION

Supermassive black hole formation is an outstanding question in astrophysics. The compelling evidence that links supermassive black holes’ evolution to that of their host galaxies (e.g. Magorrian et al. 1998; Ferrarese & Merritt 2000; Tremaine et al. 2002; Marconi & Hunt 2003; Häring & Rix 2004; Gültekin et al. 2009; McConnell & Ma 2013) strongly suggests that the answer must be sought in the broader context of galaxy assembly.

A few different formation scenarios have been proposed. Supermassive black hole seeds might have a classical stellar origin as the leftover of the first generation of stars (e.g. Madau & Rees 2001; Volonteri, Haardt & Madau 2003; Tanaka & Haiman 2009) or they might represent the outcome of the core collapse of primordial nuclear star clusters (e.g. Quinlan & Shapiro 1990; Devecchi & Volonteri 2009; Davies, Miller & Bellovary 2011; Devecchi et al. 2012; Lupi et al. 2014). Both proposals, however, face difficulties in explaining the few observational constraints available, namely the early occurrence of massive ($\gtrsim 10^9$ – $10^{10} M_{\odot}$) accreting black holes in $z \sim 6$ – 7 quasars (Fan et al. 2006; Mortlock et al. 2011; but see also Treister et al. 2013). The main reason is that both scenarios tend to predict small seeds (up to $\sim 1000 M_{\odot}$ at most) which are

unlikely to grow fast enough to power those high- z quasars, unless sustained super-Eddington accretion is advocated (e.g. Johnson & Bromm 2007; Pelupessy, Di Matteo & Ciardi 2007; Milosavljević et al. 2009; Alexander & Natarajan 2014; Madau, Haardt & Dotti 2014; Volonteri, Silk & Dubus 2015).

Although these observational constraints do not necessarily rule out those mechanisms on a physical base, they may more easily be explained by the so called ‘direct collapse’ scenario (e.g. Bromm & Loeb 2003; Begelman, Volonteri & Rees 2006; Lodato & Natarajan 2006; Dijkstra et al. 2008; Begelman & Shlosman 2009; Latif et al. 2013; Mayer et al. 2015). This latter envisages a large mass of pristine gas ($\sim 10^6$ – $10^7 M_{\odot}$), promptly accumulated at the centre of a galaxy-sized halo on (sub)parsec scales. A large fraction of it would rapidly ($<10^6 \text{ yr}$) form a massive seed (10^4 – $10^6 M_{\odot}$), directly at the centre of a galaxy at $z \sim 15$. Attractive as it is, this process is far from being proved and at least two major steps require further investigations.

Although in principle there is plenty of gas available at high redshift and cold flows have been shown to be effective in bringing that gas down to the centre of (massive) haloes (Di Matteo et al. 2012), the conditions to avoid substantial fragmentations and to overcome the centrifugal barrier are not fully understood yet. Several possibilities have been discussed, such as the dissociation of H_2 molecules by Lyman–Werner ionizing radiation coming from nearby, star-forming galaxies in order to avoid cooling and

*E-mail: fiacconi@physik.uzh.ch (DF); emr@strw.leidenuniv.nl (EMR)

fragmentation (Ferrara & Loeb 2013; Dijkstra, Ferrara & Mesinger 2014; Agarwal et al. 2014, 2015). Another possibility is the onset of supersonic turbulence and the removal of angular momentum due to non-axisymmetric perturbations and gravitational torques during the collapse of the halo (Begelman & Shlosman 2009; Choi, Shlosman & Begelman 2013, 2015), or at the centre of major merger remnants between rare and massive galaxies at high redshift (Mayer et al. 2010, 2015).

The second issue is how to actually form a black hole and what is its initial mass. The answer may vary according to the physical properties of the assembled mass. When more than $\sim 10^8 M_\odot$ can be rapidly piled up, the resulting structure likely becomes dynamically unstable (even if rotating) and relativistic radial instability can lead to implosion and direct black hole formation (Fowler 1966; Baumgarte & Shapiro 1999; Shibata & Shapiro 2002). However, forming such a structure requires rather extreme conditions (e.g. a major merger; Mayer et al. 2015). With relatively milder accretion rates, nuclear burning can start at the centre of a convectively stable object, i.e. a supermassive star (Begelman 2010). After a million years, the core that could not convectively acquire fresh hydrogen collapses to form a stellar size ($\sim 100 M_\odot$) black hole. Highly optically thick gas keeps however falling on to the newly born black hole, with enough angular momentum to be able to generate accretion power. This energy feedback inflates the innermost part of this inflow, creating a *quasi-star*: a massive, slowly rotating envelope, sustained against its own gravity by the black hole accretion power (Begelman, Rossi & Armitage 2008; Begelman 2010; Volonteri & Begelman 2010; Ball et al. 2011; Dotan, Rossi & Shaviv 2011). At quasi-star centres, the embryo black holes may accrete at a super-Eddington rate, as energy is transported outwards by convection (not by radiative diffusion) through the envelope. The initial expectation was that seeds of $\sim 10^4$ – $10^5 M_\odot$ may easily grow in $\lesssim 1$ Myr (Begelman et al. 2008). After this time, the envelope would be definitively dispersed and accretion would proceed at an Eddington limited fashion directly from the protogalactic disc.

This result was questioned by Dotan et al. (2011), that tried to quantify the impact of radiative driven winds from the surface of these weakly bound envelopes. They found that in a large part of the black hole mass-envelope mass parameter space, winds can be so powerful that the envelope evaporates before the black hole is able to double its mass. This effect would greatly limit the number of protogalaxies in whose centre the conditions are prone to massive $> 10^4 M_\odot$ seed formation. Moreover, because in their model most of the radiation energy in diffusive luminosity is converted into kinetic energy of the wind, quasi-stars would be very dim objects, virtually undetectable. In that paper, however, the radiative driven wind was not modelled solving the full equations of motion and in particular, the advection energy term was neglected.

We therefore set out to critically reconsider continuum driven winds from the surface of radiation-dominated objects. In fact, we find that the advection term has an important dynamical role as the main driver of the wind. We then explicitly consider quasi-stars and calculate mass-loss rates and photospheric properties and we assess their detectability with *Hubble Space Telescope* (HST) and the James Webb Space Telescope (JWST). Our result is that although winds are still a major limit for black hole growth, photospheric luminosities in the wind ensure possible bright targets (10^{44} – 10^{46} erg s $^{-1}$) for JWST.

This paper is organized as follows: in Section 2, we describe our model of radiation-dominated wind and we discuss the main properties; in Section 3, we couple this wind prescription to the hydrostatic envelope predicted for quasi-stars, finding equilibrium

solution and discussing their evolution. Section 4 is devoted to simple predictions regarding the observability of quasi-stars by current and future space-based telescopes. We discuss and summarize our main findings in Section 5, addressing the main limitations of our work and future steps.

2 THE WIND MODEL

2.1 Equations and general properties

We consider a stationary, spherically symmetric, radiation-dominated wind launched by a non-rotating, stellar-like object of mass M_* from a spherical surface of radius R_* , that represents the base of the wind¹. By radiation-dominated, we mean that the contribution of the gas pressure p_{gas} is assumed to be negligible compared to the radiation pressure p_{rad} , i.e. $p_{\text{gas}}/p_{\text{rad}} \ll 1$. This assumption allows us to neglect the presence of p_{gas} in the following calculations (and we simply write $p \equiv p_{\text{rad}}$), but it requires at the same time that the wind is launched from a radiation-dominated object (as we consistently show for quasi-stars in Section 3). Just outside R_* , the gas is assumed to be initially optically thick and interacts with radiation through a constant opacity κ . In this section, we implicitly assume the Thompson scattering opacity (though the specific value is in fact irrelevant for our results since we develop all our calculations in a dimensionless form), while in Section 3 we will adopt a temperature-dependent opacity law (see Section 3.1). We stress, however, that the (dynamical) results presented in this section are largely independent of the assumed opacity law, as also discussed in Section 3.3. We are interested in primordial composition objects, where line-driven interaction is negligible. The equations that describe this system are similar to those used by several previous works about stellar winds (and spherical accretion) in both the optically thin and optically thick regime (e.g. Żytkow 1972; Begelman 1978, 1979; Kato 1983; Quinn & Paczynski 1985):

$$\dot{M} = 4\pi r^2 \rho v, \quad (1)$$

$$\frac{1}{2} \frac{dv^2}{dr} = -\frac{GM_*}{r^2} + \frac{\kappa L}{4\pi r^2 c}, \quad (2)$$

$$\dot{M} \frac{d}{dr} \left(\frac{v^2}{2} - \frac{GM_*}{r} + \frac{p+U}{\rho} \right) = -\frac{dL}{dr}. \quad (3)$$

These equations determine the structure of the gas density ρ , the radial gas velocity v , the luminosity carried by photons L , the (radiation) pressure p and the (radiation) internal energy density U as a function of the spherical radius r within the gravitation potential $\Phi = -GM_*/r$ induced by M_* outside R_* . The steady-state wind is characterized by the constant outflow rate \dot{M} . Equations (1), (2) and (3) describe the conservation of mass, momentum, and energy, respectively.

Such a system of equations is not closed and several approaches can be used to close it to different degrees of approximation. Shaviv (2001a) and Owocki, Gayley & Shaviv (2004) start from similar equations, except that they initially include the contribution of the gas thermal pressure to the momentum and energy conservation. Then, they simplify the system focusing on the supersonic branch, thus subsequently neglecting the gas pressure terms in the momentum equation (which brings it back to our same equation 2) and the

¹ In the following, we will always use the subscript $*$ to indicate quantities evaluated at R_* .

advection term $(p + U)/\rho$ (with the corresponding one due to gas pressure) in the energy equation. This approximation leads to the great advantage that fully analytic solutions can be derived. However, the limitation is that the lack of the advective term makes the behaviour of the wind insensitive to the local optical thickness.

Instead, we follow an approach similar to that used by e.g. Quinn & Paczynski (1985) and we explicitly include additional prescriptions to properly describe the behaviour of the wind in the extrema of very optically thin and optically thick regime, i.e. when the optical depth:

$$\tau(r) = \int_r^{+\infty} \kappa \rho(x) dx, \quad (4)$$

is either $\tau \ll 1$ or $\tau \gg 1$, respectively. When the wind is optically thick, radiation and matter can reach local thermodynamical equilibrium at the same temperature T (which relates to the energy density $U = 3p = aT^4$, where a is the radiation constant) and the gradient of the radiation energy density is

$$\left. \frac{dU}{dr} \right|_{\tau \gg 1} = -\frac{3\kappa\rho L}{4\pi r^2 c}. \quad (5)$$

On the other hand, local thermodynamical equilibrium may not be reached in the optically thin limit and a unique temperature may not be a physically motivated quantity. In this case, the photons carrying L travel with roughly radial orbits and interact very little with matter, keeping L almost constant (see e.g. Żytkow 1972). Then, the radiation energy density decreases mostly because of geometrical dilution in a progressively larger volume:

$$\left. \frac{dU}{dr} \right|_{\tau \ll 1} = -\frac{L}{2\pi r^2 c}. \quad (6)$$

We follow Quinn & Paczynski (1985) in defining the total gradient of U as the sum of the two limiting cases:

$$\frac{dU}{dr} = -\frac{L}{2\pi r^2 c} f(\tilde{\tau}), \quad (7)$$

where we define the function

$$f(\tilde{\tau}) = \frac{3\tilde{\tau}}{2} + 1, \quad \tilde{\tau} \equiv \kappa \rho r. \quad (8)$$

The ‘effective’ opacity $\tilde{\tau}$ leads the gradient of U to the right optically thin and optically thick limits when $\tilde{\tau} \ll 1$ and $\tilde{\tau} \gg 1$, respectively. However, $\tilde{\tau}$ is just an approximation of the actual opacity τ ; the two are related by a constant factor when τ is a power law and such a factor is close to 1 when $\tau \propto r^{-1}$. Although we do not know a priori the relationship between τ and $\tilde{\tau}$, we demonstrate in the following that $\tau \propto r^{-1}$ roughly holds and therefore $\tilde{\tau} \simeq \tau$ (see Section 3).

Finally, we need to relate p and U to close the system of equations. Quinn & Paczynski (1985) implicitly assume that $p = U/3$ everywhere in the flow (see their equations 11 b and 12). This is correct in the optically thick regime, but is not valid when the gas is optically thin. Indeed, $U = p$ when the gas is optically thin; this different relation between p and U is also responsible for the inexact relation between the luminosity observed by an observer at infinity and by an observer comoving with the flow, as reported by Quinn & Paczynski (1985; see also Section 2.2 and Cassinelli & Castor 1973). In order to have a smooth transition between the two regimes, similar to the case of the gradient of U (see equation 7), we propose the following functional form for the opacity-dependent ratio p/U :

$$\frac{p}{U} \equiv g(\tilde{\tau}) \equiv \left(\frac{3\tilde{\tau}}{2} + 1 \right) \left(\frac{9\tilde{\tau}}{2} + 1 \right)^{-1}. \quad (9)$$

Fig. 1 shows the behaviour of both $f(\tilde{\tau})$ and $g(\tilde{\tau})$.

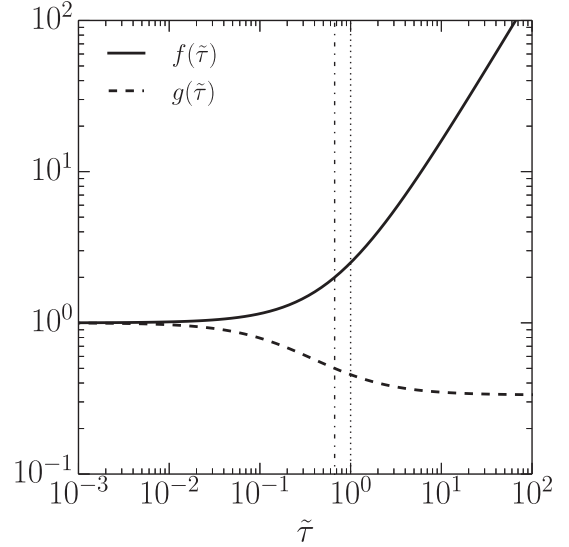


Figure 1. The tick continuous and dashed lines show the behaviour of f and g as a function of $\tilde{\tau}$, respectively. For reference, the vertical dotted and dashed lines mark the points $\tilde{\tau} = 1$ and $2/3$, respectively.

The latter goes correctly from 1 (when the wind is optically thin) to $1/3$ (when the wind is optically thick). However, the accuracy of both prescriptions is questionable around $\tilde{\tau} \sim 1$, because the actual form is largely arbitrary. We therefore compute and compare wind models, choosing different functional form for $f(\tilde{\tau})$ and $g(\tilde{\tau})$ and concluded that our results are not affected as long as the limits are correct and the transition occurs rapidly (over several $\tilde{\tau}$) around $\tilde{\tau} \sim 1$.

The equation of the conservation of energy can be directly integrated, becoming an algebraic equation for L :

$$L(r) = \dot{E} - \dot{M} \left(\frac{v^2}{2} - \frac{GM_*}{r} + (1 + g(\tilde{\tau})) \frac{U}{\rho} \right), \quad (10)$$

where we make use of $g(\tilde{\tau})$ explicitly and we introduce the total conserved luminosity \dot{E} , which represents the constant of integration. The system of equations that we finally solve (often dubbed as ‘wind equations’ in the following) is composed of equations (1), (2), (7) and (10), coupled with the definitions of $\tilde{\tau}$, $f(\tilde{\tau})$ and $g(\tilde{\tau})$. The system has two ordinary differential equations and two algebraic equations for the dependent variables ρ (or $\tilde{\tau}$), v , L and U as a function of r .

At this point, it is convenient to introduce new dimensionless variables. We define the new velocity variable $w = v^2/v_{\text{esc}}^2$, where $v_{\text{esc}}^2 = 2GM_*/R_*$ is the escape velocity from the base of the wind, the new radiation energy density variable $u = U\kappa R_*^2/(GM_*)$, and the new luminosity variable $\Gamma = L/L_{\text{Edd}}$. Γ is the Eddington ratio and the Eddington luminosity L_{Edd} is defined as

$$L_{\text{Edd}} = \frac{4\pi c GM_*}{\kappa} = 1.26 \times 10^{38} \bar{\kappa}^{-1} m_* \text{ erg s}^{-1}, \quad (11)$$

where $\bar{\kappa}$ is the opacity in units of the electron scattering opacity $\kappa_{\text{es}} = 0.35 \text{ cm}^2 \text{ g}^{-1}$ (assuming primordial abundances) and m_* is the stellar mass M_* in units of solar masses. The independent variable r can also be transformed into $x = 1 - R_*/r$, such that the interval $r \in [R_*, +\infty)$ is mapped into $x \in [0, 1)$. We can first express equation (2) with the new variables as

$$w' = \Gamma - 1, \quad (12)$$

where here and in the following $' = d/dx$. The gradient of the radiation energy density u becomes

$$u' = -2(1-x)\Gamma f(\tilde{\tau}), \quad (13)$$

where $f(\tilde{\tau})$ is defined in equation (8) and

$$\tilde{\tau} = \frac{\alpha\beta}{w^{1/2}}(1-x), \quad (14)$$

is the definition of $\tilde{\tau}$ using our dimensionless variables. We introduce the two factors α and β ; α is a dimensionless expression for \dot{M} in terms of the trapping radius R_{tr} (Begelman 1978, 1979):

$$\alpha = \frac{R_{\text{tr}}}{R_*} = \frac{\kappa \dot{M}}{4\pi c R_*}. \quad (15)$$

The trapping radius is where the diffusion time-scale for photons is equal to the dynamical time of the outflowing wind, $R_{\text{tr}}(\tilde{\tau}/c) \approx R_{\text{tr}}/v$, which implies that $\tilde{\tau} \approx c/v$ at R_{tr} . We will see in the following that within this radius, since the radiation is *trapped*, the luminosity transported by diffusion becomes subdominant with respect to the energy advected within the flow. The parameter β is a dimensionless factor depending on the properties of the star only:

$$\beta \equiv \frac{c}{v_{\text{esc}}} \approx 486 m_*^{-1/2} r_*^{1/2}, \quad (16)$$

where r_* is the stellar radius in units of solar radii. β appears naturally from the normalization of the optical depth and measures the deepness of the gravitational potential well of the parent star. It depends on the stellar properties R_* and M_* only and therefore, M_* and β (or v_{esc}) are enough to rescale the equations in physical units. Finally, the algebraic equation for Γ can be obtained from equation (10) and reads

$$\Gamma = \dot{\mathcal{E}} - \alpha \left(w + x - 1 + \frac{1 + g(\tilde{\tau})u}{1-x} \right), \quad (17)$$

where $\dot{\mathcal{E}} = \dot{E}/L_{\text{Edd}}$ and $g(\tilde{\tau})$ is defined in equation (9). The dependent variables w , u and Γ are proportional to the kinetic energy of the gas, to the energy density of the radiation and to the luminosity carried by photons, respectively. Therefore, equations (12), (13) and (17) compose the system that describes the energy exchanges between the different components of the system.

2.2 Numerical integration of the wind equations

We integrate numerically the wind equations (equations 12, 13, 14 and 17) using the `CVODE` module of the `SUNDIALS`² package (Cohen, Hindmarsh & Dubois 1996; Hindmarsh et al. 2005). `CVODE` is a C solver for stiff and non-stiff ordinary differential equation systems in explicit form. We adopt a fifth-order backward differentiation formula in fixed-leading coefficient form with a modified Newton iteration to solve non-linear systems. `CVODE` provides also a module to find the roots of non-linear equations which is well suited to determine the position of the photosphere and the local properties of the wind while contemporary solving the wind equations.

In order to find solutions of the wind equations, we follow the procedure outlined by Quinn & Paczynski (1985; see also Żytkow 1972; Kato 1983). First of all, we characterize our star by choosing a value for β . Then, we pick a value for α and $\dot{\mathcal{E}}$. These two constants of integration are not enough to fully characterize the wind. We need a boundary condition, specifically the asymptotic gas velocity

at infinity w_∞ . With that, we can specify the initial conditions at a large radii $x_\infty = 1 - \delta$, much larger than R_* (i.e. when $\delta \rightarrow 0$) and start our integration of the wind from outside inwards. Practically, we calculate the radiative luminosity as seen by an observer at infinity as

$$\mathcal{L}_\infty = \dot{\mathcal{E}} - \alpha w_\infty. \quad (18)$$

At x_∞ , the luminosity Γ_∞ comoving with the flow can be considered constant and given by

$$\Gamma_\infty = \frac{\mathcal{L}_\infty}{1 + 2w_\infty^{1/2}/\beta} = \frac{\dot{\mathcal{E}} - \alpha w_\infty}{1 + 2w_\infty^{1/2}/\beta}. \quad (19)$$

We can then integrate the radiation energy density in the optically thin limit:

$$u' \simeq -2(1-x)\Gamma_\infty \Rightarrow u = \Gamma_\infty(1-x)^2, \quad (20)$$

where we use the boundary condition $u(1) = 0$, and the wind velocity:

$$w' = \Gamma_\infty - 1 \Rightarrow w = w_\infty - (\Gamma_\infty - 1)(1-x). \quad (21)$$

We can also write the explicit behaviour of $\tilde{\tau}$:

$$\tilde{\tau} = \frac{\alpha\beta(1-x)}{\sqrt{w_\infty - (\Gamma_\infty - 1)(1-x)}}. \quad (22)$$

Note that equation (19) comes out naturally by evaluating equation (17) at $x \rightarrow 1$, where $1 + g(\tilde{\tau}) \rightarrow 2$ and u and $\tilde{\tau}$ are described by the expressions above (equations 20 and 22). Next, we choose a value for δ , typically $\delta \sim 10^{-6}$, we check that indeed $\tilde{\tau}(x_\infty) \ll 1$ and we use the formulas above to provide the initial conditions $w(x_\infty)$ and $u(x_\infty)$ for the wind equations.

We then integrate the equations inwards up to the surface $x = 0$ (or up to the point where a solution exists). We define the photosphere as the place where the equality $L_{\text{phot}} = 4\pi R_{\text{phot}}^2 \sigma T_{\text{phot}}^4$ is satisfied, where $\sigma = ca/4$ is the Stephan–Boltzmann constant, whereas the temperature T is defined from the energy density U as $T = (U/a)^{1/4}$, regardless of the local optical depth. Such a temperature is a proxy for the local temperature and it recovers its full physical meaning only when $\tilde{\tau} > 1$. The photosphere identified in this way usually lays at $\tilde{\tau} \sim 2-3$.

Every solution of the wind equations is specified by the parameters α , $\dot{\mathcal{E}}$ and w_∞ , once the underlying star is set by β . Among those parameters, α is directly related to the outflow rate \dot{M} and is necessary to solve the wind equations, i.e. such a model does not allow to infer theoretically the value of \dot{M} a priori. However, an *acceptable* solution has to satisfy additional self-consistency requirements, which in turns impose constraints of the parameter space and ultimately on the value of \dot{M} . Those self-consistency requirements are imposed by the assumption that the wind originates from a star-like object. In particular: (i) the solution has to extend inwards to at least $x = 0$; (ii) the wind has to be optically thick close to the surface of the star, i.e. the photosphere has to be above the base of the wind, namely $\tilde{\tau}_* > 1$ and $R_{\text{phot}} > R_*$; and (iii) the wind has to connect to an hydrostatic solution, i.e. it should be initially subsonic (i.e. $\mathcal{M}_* < 1$) and with a moderate velocity³ (i.e. $w_* \ll 1$). A wind solution is then accepted only when it satisfies all the conditions listed above, and it is discarded otherwise.

² `SUNDIALS` is publicly available at <https://computation.llnl.gov/casc/sundials/main.html>.

³ As consequence of the assumption of steady-state, we note that we cannot allow for $w_* = 0$ because the density would otherwise diverge, as implied by the conservation of mass in equation (1).

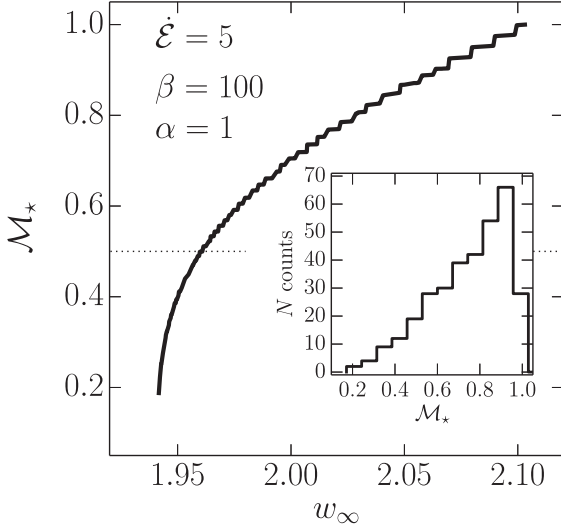


Figure 2. Relation between the velocity at infinity w_∞ and the Mach number at the surface \mathcal{M}_* assuming $\beta = 100$, $\alpha = 1$ and $\dot{\mathcal{E}} = 5$. The dotted thin line marks $\mathcal{M}_* = 0.5$ for reference. The range of possible w_∞ is very narrow. The inset shows the distribution of the Mach numbers \mathcal{M}_* obtained by 500 realizations. A clear peak around 0.8–0.9 is present.

2.2.1 The wind velocity at infinity

To try and simplify further our procedure, we first assess the sensitivity of our solution to our choice of w_∞ . The arbitrariness of w_∞ is simply a consequence of our neglecting gas pressure, in the equations describing a radiation-dominated wind. When thermal gas pressure is explicitly accounted for, the sonic point of a solution (i.e. where $\mathcal{M} = 1$) is also a critical point (i.e. a divergent point for w'). The requirement on the position of the critical point to cure the local divergency translates naturally into a condition that fixes the value of w_∞ . As a consequence, solutions of the wind equations with gas pressure only dependent on α and $\dot{\mathcal{E}}$ (e.g. Quinn & Paczynski 1985). In our solutions, instead, the sonic point is *not* a critical point, and w_∞ is not univocally determined. However, the fact that with gas pressure terms there is only a single value for w_∞ and that solutions should be continuous as $p_{\text{gas}}/p_{\text{rad}} \rightarrow 0$ suggests that the range of possible w_∞ may be narrow. Therefore, we investigate this possibility.

We setup a grid of five representative values for $\beta \in \{10, 50, 100, 500, 1000\}$, and five representative values for $\dot{\mathcal{E}} \in \{1.5, 2.5, 5, 7.5, 10\}$. For each pair $(\beta, \dot{\mathcal{E}})$, we divide the interval $\log \alpha \in [-3, 1]$ uniformly, and for each value of α we run 10^3 integrations of the wind equations choosing a random value for w_∞ distributed uniformly in the logarithmic interval $[-3, \log(\dot{\mathcal{E}}/\alpha)]$. We keep only the acceptable solutions according to Section 2.2.

Our results confirm that the range of w_∞ that leads to self-consistent solutions is narrow, usually $\lesssim 0.1$ dex, and centred around $w_\infty \sim 1$. The values of w_∞ also correlate with \mathcal{M}_* in the interval $0.1 \lesssim \mathcal{M}_* < 1$. Such a correlation is shown for 500 realizations in Fig. 2 for an example configuration with $\beta = 100$, $\alpha = 1$ and $\dot{\mathcal{E}} = 5$ and exhibits typical features common to all the other combinations of parameters. In particular, most of the interval of allowed w_∞ corresponds to values of the Mach number larger than ~ 0.5 – 0.6 , as shown by the distribution of \mathcal{M}_* represented in the inset of Fig. 2, peaking around $\mathcal{M}_* \sim 0.8$. Motivated by that, we can use this occurrence as an approximate additional constraint to remove the freedom of choosing w_∞ by choosing a value for \mathcal{M}_* to be

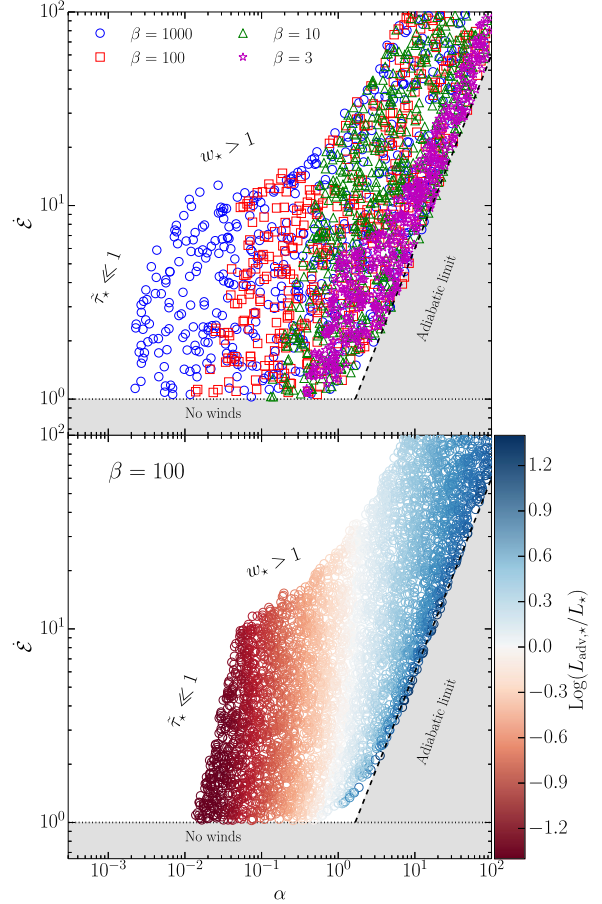


Figure 3. Monte Carlo sampling of the parameter space $\alpha - \dot{\mathcal{E}}$. Upper panel: blue circles, red squares, green triangles and magenta stars show the results for $\beta = 1000, 100, 10$ and 3 , respectively. For visualization purposes, we show 10 per cent of the 10^4 calculations performed for each value of β . Lower panel: the same as above showing all the results for the case $\beta = 100$ where we colour-coded the points according to the ratio between the advected luminosity at the surface $L_{\text{adv},*}$ and the radiative luminosity L_* at R_* . Both panels show the limits to the parameter space imposed by the self-consistency conditions as described in the text.

matched at R_* . In the following, we focus only on solutions with $\mathcal{M}_* = 0.8 \pm 0.05$.

2.3 Results

We are now in the position to explore the properties of the solutions within the parameter space $(\alpha, \dot{\mathcal{E}})$ as a function of β . Fig. 3 highlights the boundaries on the parameter space imposed by the self-consistency conditions. Solutions are limited from below by the requirement that $\dot{\mathcal{E}} \geq 1$. We assume this condition as necessary in order to launch the wind. In fact, the actual condition to have an accelerating wind is $\Gamma_* > 1$ or in other words, that the star should shine above the Eddington limit (equation 12). None the less, we conveniently chose the limit $\dot{\mathcal{E}} \geq 1$ because (i) it implies $\Gamma_* > 1$ and (ii) the hydrostatic solution (the star) below the wind naturally provides $\dot{E} \approx L_*$ as a boundary condition (we discuss this point with more details in Section 3). The limit at small α and $\dot{\mathcal{E}} \lesssim 10$ results from imposing $\tau_* > 1$ and it depends on β since the normalization of the optical depth is $\propto \alpha\beta$, as shown by equation (14) and in the upper panel of Fig. 3. Physically, this is because matter needs to be faster to escape from a more compact star, and from mass conservation

($\rho \propto \dot{M}/v$) it follows that a higher mass-loss rate is required to maintain the same optical depth $\bar{\tau}_* > 1$. Finally, at fixed α , the upper value of $\dot{\mathcal{E}}$ is constrained by the matching with a hydrostatic solution below the wind, that requires $w_* < 1$. Incidentally, we note here that our set of prescriptions do not set an upper limit on \dot{E} . This will be provided by the physical characteristics of the stellar object powering the wind, more explicitly by how much super Eddington its emission can be. We will explicitly show this in Section 3 for quasi-stars.

The maximum mass-loss rate for a given $\dot{\mathcal{E}}$ (grey area on the right) is instead a physical limit. This is obtained when the dominant energy source for the kinetic luminosity of the wind is the enthalpy of the gas and $\dot{\mathcal{E}} \approx w_\infty \alpha$. In practise, this is the behaviour of an adiabatic wind. We show this by considering a fully adiabatic solution. This latter has no radiative luminosity in its governing equations (see Appendix A), and the presence of a critical point allows us to relate the velocity at infinity $w_{\infty, \text{adiab}}$ to the condition at the base of the wind. We can therefore derive that an adiabatic wind with $\mathcal{M}_* = 0.8$ will have $w_{\infty, \text{adiab}} = 3w_c \approx 0.6$, where w_c is the velocity at the critical point $w_c = s_c$, related to \mathcal{M}_* by equation (A4) and the relation plotted in Fig. A1. For a given $\dot{\mathcal{E}}$, we therefore have

$$\alpha_{\text{max}} \approx \dot{\mathcal{E}}/0.6. \quad (23)$$

This relation is plotted as a dashed line in Fig. 3 and clearly marks the rightmost limit of our solutions and the beginning of the ‘forbidden’ region dubbed ‘adiabatic limit’.

That our solutions tend towards an adiabatic behaviour as \dot{M} increases, can be better appreciated by looking at the lower panel of Fig. 3, which shows solutions for $\beta = 100$, colour coded according to the ratio $L_{\text{adv},*}/L_*$, where $L_{\text{adv}} = \dot{M}(p + U)/\rho$ is the luminosity advected within the bulk outflow. Across $\alpha \sim 1$, the regime of the wind changes: for $\alpha < 1$ energy in radiation is mainly transported by diffusion while for $\alpha > 1$ advection becomes more and more dominant as the outflow rate increases towards the adiabatic limit. As mentioned before, this is exactly the physical meaning of the trapping radius (see also Fig. 4, lower rightmost panel) and $\alpha > 1$ implies that the trapping radius occurs within the outflow, $R_{\text{tr}} > R_*$ (see equation 15). Formally, a fully adiabatic solution has $R_{\text{tr}} = \infty$ (i.e. $\alpha = \infty$) and correspondently $L_{\text{adv},*}/L_* = \infty$. Advection is indeed the only transport mechanism in an adiabatic wind. We can go a step further and calculate \dot{M} of a solution *relative* to the maximum possible mass-loss rate. The latter corresponds to that of an adiabatic wind (\dot{M}_{ad} , equation A7) launched from the same star, with the same initial conditions (i.e. the same $c_{s,*}$ and ρ_* at R_*) at the same $\dot{\mathcal{E}}$ (which for an adiabatic wind reads $\dot{\mathcal{E}} = \dot{M}_{\text{ad}}(v_*^2/2 + 3c_{s,*}^2 - GM_*/R_*)/L_{\text{Edd}}$)

$$\frac{\dot{M}}{\dot{M}_{\text{ad}}} \approx \left(1 - \frac{L_*}{\dot{E}}\right). \quad (24)$$

When the contribution of the radiative luminosity L_* at R_* to the total energetic budget becomes negligible, \dot{M} approaches the adiabatic value.

The upper panel of Fig. 3 shows the comparison of 10^4 realizations for four different values of β . We find that the winds originating

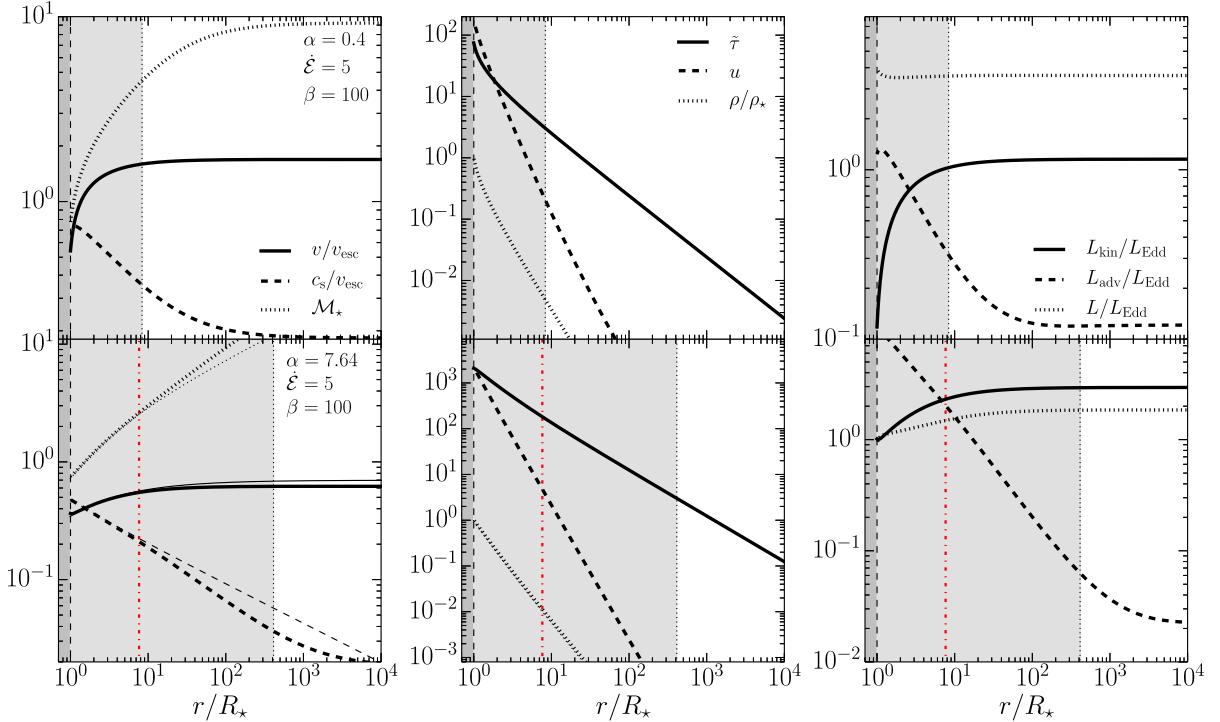


Figure 4. Example solutions of the wind equations for $\beta = 100$. The upper row shows the solution for $\alpha = 0.4$ and $\dot{\mathcal{E}} = 5$, while the bottom row shows the solution for $\alpha = 7.64$ and $\dot{\mathcal{E}}$, very close to the adiabatic limit of Fig. 3. Left-hand column: continuous, dashed and dotted lines show the profile of v/v_{esc} , c_s/v_{esc} and \mathcal{M}_* , respectively. Central column: continuous, dashed and dotted lines show the profile of $\bar{\tau}$, u and ρ/ρ_* , respectively. Right-hand column: continuous, dashed and dotted lines show the profile of $L_{\text{kin}}/L_{\text{Edd}}$, $L_{\text{adv}}/L_{\text{Edd}}$ and L/L_{Edd} , respectively. The dark and light grey shaded regions in all panels mark the base of the wind and the surface of the photosphere, respectively, while the red, vertical, dash-dotted lines in the bottom row indicate the position of the trapping radius. The thin lines in the bottom-left panel and the thin dotted line in the bottom-central panel show the velocity, sound speed, Mach number and density, respectively, of the adiabatic wind with the same critical point of the wind solution. The two solutions are very similar within R_{tr} .

from more compact stars (i.e. those with smaller β) sustain higher outflow rates at the same total luminosity $\dot{\mathcal{E}}$. This is again related to the fact that gas needs to be faster to escape from a more compact star, and it compensates this increase in velocity by an increase in \dot{M} to maintain optical thickness. As a consequence, an *optically thick* wind needs to carry a larger and larger fraction of the total luminosity in kinetic and advective form. This explains why the range of possible \dot{M} gets squeezed towards the adiabatic limit for⁴ $\beta \rightarrow 1$.

Fig. 4 shows two example solutions of the wind equations with $\beta = 100$. The upper row shows a solution with $\alpha = 0.4$ and $\dot{\mathcal{E}} = 5$, i.e. at the centre of the allowed region in the lower panel of Fig. 3, while the bottom row shows a solution with $\alpha = 7.64$ and $\dot{\mathcal{E}} = 5$, i.e. very close to the adiabatic limit. The wind velocity of the first solution grows steeply within the photosphere and then flattens to its asymptotic values; on the contrary, the sound speed c_s decreases quickly within the photosphere, matching the gas velocity at the sonic point very close to R_* , beyond which the wind becomes highly supersonic. Note that, regardless of the optical depth, we always use the general definition of sound speed:

$$c_s^2 = \left(\frac{\partial p}{\partial \rho} \right)_S = \frac{4}{3} \frac{p}{\rho}, \quad (25)$$

where S is the specific entropy and the second equality is based on the most general equation of state for a non-isentropic, radiation-pressure dominated fluid, namely $p(\rho, S) = K(S)\rho^{4/3}$. In fact, this relation is only valid when $p = U/3$, i.e. in the optically thick limit, but we need to consider the behaviour of c_s only within the photosphere. The solution close to the adiabatic limit shows a similar behaviour, though the gas velocity grows less steeply than in the previous case and mostly within R_{tr} . It also reaches an asymptotic velocity lower than the previous case, though the total energy $\dot{\mathcal{E}}$ is the same.

The profiles of the optical depth, density and radiation energy density are similar in both examples. We can fairly accurately describe them with power laws, at least close to and outside the photosphere. In particular, the optical depth decreases with radius as r^{-1} , while the density as r^{-2} once the gas velocity remains almost constant. This confirms a posteriori that $\bar{\tau}$ is a good approximation for τ . We note also that the wind is highly optically thick close to R_* , while the photosphere forms at $\bar{\tau}_{\text{phot}} \sim 2-3$. This latter confirms that our approximate treatment of the transition between the optically thin and thick regimes gives sensible results, close to the conventional $\tau_{\text{phot}} \approx 1$.

The largest difference between the two solutions is in the energy budget, shown in the left column of Fig. 4. There, we compare the profiles of the radiative luminosity L , the advected luminosity L_{adv} , and the kinetic luminosity $L_{\text{kin}} = \dot{M}v^2/2$, all normalized to L_{Edd} for convenience. These luminosities, summed up with $-G\dot{M}M_*/r$, give the total, constant luminosity $\dot{\mathcal{E}}$. The energy budget in the first solution is dominated by the radiative luminosity from the base of the wind (indeed $R_{\text{tr}} < R_*$) to infinity. After a small decrease, it remains almost constant with radius, while L_{kin} quickly rises within the photosphere, yet remaining subdominant. This behaviour indicates that the acceleration of the wind is not powered by L but it rather occurs at the expenses of L_{adv} , that drops accordingly within the photosphere. In contrast, L_{adv} in the $\alpha = 7.64$ case (lower

panel) is initially an order of magnitude higher than both L and L_{kin} and becomes comparable to L around R_{tr} . Instead, L remains always subdominant compared to L_{kin} . The radiative luminosity's mild growth within the photosphere is similar to that of an 'effective' Eddington ratio that one would obtain from equation (12), $\Gamma_{\text{eff}} = 1 + w'$, when w' from the adiabatic equations (A1) and (A2) is used. Notably, also in this case, L_{kin} is ultimately powered by L_{adv} .

Finally, we show explicitly the similarity between the solution close to the adiabatic limit and an actual adiabatic solution in the bottom row of Fig. 4. Specifically, after calculating the solution of our wind equations, we calculate also the adiabatic solution (see Appendix A) which has the same critical radius. Such an adiabatic solution crosses naturally the critical point with the same value of critical velocity w_c of the full solution, and closely resembles it (comparing v , c_s , \mathcal{M} , and ρ) within the trapping radius, outside of which radiative diffusion becomes relevant.

From our results, it is clear that the ultimate source of kinetic energy for the gas is advection energy and *not* the diffusive radiation luminosity. This is not consumed as the gas propagates outwards. To increase the mass-loss, it is therefore necessary to go towards an adiabatic solution, where initially the advection energy dominates the energy budget. This is different from the results by Shaviv (2001a), Owocki et al. (2004), and from the description used in Dotan et al. (2011) of a 'photon-tired' wind.

3 WINDS FROM QUASI-STARS

Directly forming massive black hole seeds is possible in principle when a mass of $\sim 10^8 M_{\odot}$ can be collected in $\sim 10^6$ yr, requiring inflow rate $> 100 M_{\odot} \text{ yr}^{-1}$. The reason is that such a rapid accumulation of mass has to occur before nuclear reactions dominate the evolution, setting a lifetime of $\sim 10^6$ yr (Begelman 2010). In these extreme conditions, a dynamical instability due to relativistic effects may develop and even rotation cannot prevent the cloud from collapsing directly into a black hole (Fowler 1966; Baumgarte & Shapiro 1999; Shibata & Shapiro 2002; see however Ferrara et al. 2014). On the other hand, milder conditions (e.g. inflow rate $\sim 0.1-1 M_{\odot} \text{ yr}^{-1}$) would lead to the formation of a supermassive star, possibly $\sim 10^5-10^7 M_{\odot}$, stabilized by some rotation (Begelman 2010; Hosokawa, Omukai & Yorke 2012; Hosokawa et al. 2013). After $\sim 10^6$ yr, a small embryo seed ($\lesssim 100 M_{\odot}$) can form at the centre of a supermassive star at the end of the hydrogen-burning phase (Begelman 2010). Such a seed then needs to go through a phase of vigorous super-Eddington accretion to reach $10^4-10^5 M_{\odot}$ within a few million years from its birth. This super-Eddington accretion can occur within a quasi-star: a very massive ($> 10^5-10^6 M_{\odot}$) quasi-hydrostatic envelope that surrounds the black hole and feeds it at a rate equal to roughly its own (i.e. quasi-star's) Eddington limit (Begelman et al. 2008). Accretion around the Eddington limit involves radiation-dominated gas, which is loosely bound with a total energy close to zero. For this reason, outflows can easily form. Here, we investigate whether this vigorous accretion in quasi-stars is also accompanied by mass-loss, as expected in other super-Eddington systems such as discs (Blandford & Begelman 2004).

3.1 Equations

We follow Begelman et al. (2008) and Dotan et al. (2011) to describe the hydrostatic envelope of a quasi-star and then we match it with our wind model, looking for equilibrium solutions. A quasi-star is made of four components: (i) the central, accreting black hole, (ii) a convective, radiation-pressure dominated envelope, (iii) a

⁴ Formally, such a limit cannot be reliably modelled by our wind equations, because it would imply approaching a regime where general relativistic corrections might become relevant.

porous radiative layer, and (iv) a wind. In the following, we briefly describe components (i)–(iii), remanding to Dotan et al. (2011) for additional details. We do not model explicitly the inflow on to the central black hole; instead, we treat it as a boundary condition, assuming that a black hole of mass M_\bullet is accreting through a convection-dominated disc (Igumenshchev & Abramowicz 1999; Stone, Pringle & Begelman 1999; Quataert & Gruzinov 2000; Agol et al. 2001) within a few Bondi radii $r_B = GM_\bullet/(2c_{s,c}^2)$, where $c_{s,c}$ is the central sound speed $\lesssim r_B$. We assume that the black hole is radiating at a luminosity L_\bullet close to the maximum that convection-dominated accretion flows can sustain evaluated at $5r_B$, namely

$$L_\bullet = L_{\text{conv}}(5r_B) = 4\pi (5r_B)^2 \rho_c c_{s,c}^3, \quad (26)$$

where ρ_c is the central density outside a few r_B . L_\bullet , it is injected at the centre of the envelope and transported till the base of the wind, first by convection and then by diffusion. We used it as an inner boundary condition for the integration of the envelope and we also neglect the gas mass within $5r_B$, assuming that only M_\bullet contributes at smaller radii. We checked the effect of varying the position of the inner boundary. We find that most of the properties in the M_\bullet – M_\star plane (see Section 3.3) remain unchanged. However, as discussed by Ball et al. (2011) and Ball, Tout & Żytkow (2012), changing the inner radius modifies (at the same central pressure) the ratio M_\bullet/M_\star of two consistent solutions. This slightly displaces the no-hydrostatic-solution region. Although a few Bondi radii are a reasonable estimate for the inner accretion region where the black hole gravity is expected to dominate, we caution that such a choice remain somewhat arbitrary.

Outside $5r_B$, the radiation-pressure dominated, convective envelope extends; we assume that it satisfies the hydrostatic equilibrium

$$\frac{dP}{dr} = -\frac{GM(r)\rho}{r^2}, \quad (27)$$

where the total pressure P is the sum of the gas pressure $P_g = \rho k_B T / (\mu m_p)$ and the radiation pressure $P_r = aT^4/3$, specified by the gas density ρ and temperature T . k_B , a and m_p are the Boltzmann constant, the radiation constant and the mass of the proton, respectively. We assume the mean molecular weight $\mu = 0.59$, appropriate for gas with primordial composition at $T > 10^4$ K, as usually true everywhere in the interior of quasi-stars. The enclosed mass $M(r)$ is given by

$$M(r) = M_\bullet + 4\pi \int_{5r_B}^r \rho(r') r'^2 dr'. \quad (28)$$

The dominant energy transport mechanism within the envelope is convection, which induces a temperature gradient very close to adiabatic; therefore, we evolve the temperature gradient assuming that it is equal to the adiabatic one:

$$\frac{d \log T}{d \log P} = \frac{\gamma_{\text{ad}} - 1}{\gamma_{\text{ad}}}, \quad (29)$$

where the adiabatic index γ_{ad} depends on the ratio $\zeta \equiv P_g/P$ according to

$$\gamma_{\text{ad}} = \frac{32 - 24\zeta - 3\zeta^2}{24 - 18\zeta - 3\zeta^2}. \quad (30)$$

The convective envelope extends till the radius r_{conv} where $L_{\text{conv}}(r_{\text{conv}}) = L_\bullet$. Outside r_{conv} , $L_{\text{conv}} < L_\bullet$ and diffusion becomes more efficient in transporting L_\bullet than convection. However, L_\bullet may be larger than the local Eddington limit associated with the local enclosed mass $M(r)$ and to electron scattering opacity. In such a condition, the gas becomes locally unstable and develops inhomogeneities (Shaviv 2001b) that have the effect of reducing the

effective opacity with respect to its microscopic value even before than the Eddington limit is reached. Following Dotan et al. (2011), we model the effective opacity κ_{eff} as

$$\kappa_{\text{eff}} = \begin{cases} \frac{\kappa}{\Gamma} \left(1 - \frac{0.16}{\Gamma}\right) & \Gamma > 0.8, \\ \kappa & \Gamma \leq 0.8, \end{cases} \quad (31)$$

where $\Gamma = L_\bullet/L_{\text{Edd}}$ is the local Eddington ratio calculated using equation (11) with $M(r)$, while κ is the microscopic opacity

$$\kappa(T) = \frac{\kappa_{\text{es}}}{1 + (T/T_0)^{-13}}, \quad (32)$$

where $T_0 = 8000$ K. This opacity models the results for pristine gas by Mayer & Duschl (2005). The effective opacity corresponds to an effective Eddington ratio $\Gamma_{\text{eff}} = 1 - 0.16/\Gamma$ when $\Gamma > 0.8$, i.e. the gas is effectively sub-Eddington, though it would be super-Eddington with the microscopic opacity. Throughout this radiative layer (that usually encompasses a tiny fraction of the total mass), we assume once again hydrostatic equilibrium (being effectively sub-Eddington) and we solve equations (27) and (28), but we evolve the temperature by mean of the radiative gradient with κ_{eff}

$$\frac{dT}{dr} = -\frac{3\kappa_{\text{eff}}\rho L_\bullet}{16\pi a c r^2 T^3}. \quad (33)$$

The luminosity L_\bullet remains constant since no energy sources/sinks are present within the convective envelope or the radiative layer. The inhomogeneities in the radiative layer can maintain the luminosity sub-Eddington as long as they remain optically thick. Since those inhomogeneity have a size of the order of the local density scale-height, we can estimate their optical depth as $\tau_{\text{eff}} \approx \chi \rho \kappa_{\text{eff}} h$, where χ is the ionization fraction calculated from the Saha equation assuming equilibrium, and $h = |\rho/(d\rho/dr)|$ is the density scaleheight. Then, the radiative layer extends up to r_{rad} such that $\tau_{\text{eff}}(r_{\text{rad}}) = 1$. We note that ζ typically decreases quickly throughout the radiative layer, reaching values $\zeta \ll 0.01$ at r_{rad} .

We can finally solve and connect the wind model described in Section 2. In particular, we use $M_\star = M(r_{\text{rad}})$ and $R_\star = r_{\text{rad}}$. From these quantities, we can evaluate β associated with the star. As in Section 2, we do not model the initial acceleration of mass explicitly. Instead, we assume that this occurs very quickly around r_{rad} , which represent the interface between the hydrostatic part and the wind. Then, we assign $\dot{E} = L_\bullet$ to guarantee the conservation of energy at the interface, because below r_{rad} there is no net displacement of mass and the total luminosity transported is just L_\bullet . Finally, we need to specify \dot{M}_{wind} . As described in Section 2.3, we assume that the wind connect with the hydrostatic part with a fixed $\mathcal{M}_\star < 1$. At the same time, we assume continuity for the density and pressure at r_{rad} , which implies

$$\dot{M}_{\text{wind}} = 4\pi r_{\text{rad}}^2 \rho_\star \mathcal{M}_\star c_\star, \quad (34)$$

where $\rho_\star = \rho(r_{\text{rad}})$ and $c_\star = c_s(r_{\text{rad}})$ are the density and the sound speed evaluated at r_{rad} as given by the integration of the radiative layer, respectively. Once we have β , \dot{E} and \dot{M} , we can integrate the wind equations as described in Sections 2.2 and 2.3, with the only difference that we use the temperature-dependent opacity of equation (32). We evaluate it using as a proxy for the local temperature $T = (U/a)^{1/4}$, which is correct only in the optically thick part of the atmosphere. We discuss the limitations of these assumptions in Section 5.

3.2 Numerical integration

We proceed to describe the numerical strategy to solve the equations in Section 3.1, similar to what has been done by Dotan et al. (2011).

- (i) We choose the black hole mass M_\bullet .
- (ii) We choose one of the central quantity, in particular the total central pressure P_c .
- (iii) We need a second quantity to specify all the boundary conditions at the centre. Therefore, we guess the value of $\zeta_c = P_{\text{gas},c}/P_c$.
- (iv) We calculate the central quantities: $T_c = 3(1 - \zeta_c)P_c/a$, $\rho_c = P_c \zeta_c \mu m_p / (k_B T_c)$, $c_{s,c}^2 = ((4/3)(1 - \zeta_c) + (5/3)\zeta_c)P_c/\rho_c$ and $r_B = GM_\bullet/(2c_{s,c}^2)$; we evaluate L_\bullet according to equation (26).
- (v) We integrate the convective envelope, namely equations (27)–(29), from the centre ($5r_B$) outwards, until we reach r_{conv} . We actually integrate the equation in their Lagrangian form, using the enclosed mass $M(r)$ as the independent variable.
- (vi) We integrate the radiative layer equations (27), (28) and (33), assuming continuity with the convective envelope from r_{conv} till r_{rad} . We integrate the equations using P as the independent variable since it varies more than the other quantities throughout the radiative layer.
- (vii) We calculate the necessary quantities to specify the properties of the wind using the values at r_{rad} as discussed in Section 3.1, namely β , \dot{E} and \dot{M}_{wind} ; specifically, we assume $\mathcal{M}_\star = 0.8$.
- (viii) We calculate the wind solution and we check that/whether it reaches r_{rad} self-consistently as described in Section 2.2.
- (ix) We compare the density $\rho^{(\text{rad})}(r_{\text{rad}})$ obtained at the end of the integration of the radiative layer with the density $\rho^{(\text{wind})}(r_{\text{rad}})$ obtained by the wind integration and we modify ζ_c in order to match the two values.

We find empirically that the ratio $\rho^{(\text{wind})}(r_{\text{rad}})/\rho^{(\text{rad})}(r_{\text{rad}})$ crosses the value 1 extremely steeply while varying ζ_c and is not monotone far from the solution. This occurrence makes difficult to use classic methods such as bisection unless the initial guesses for the values of ζ_c that bracket the final solution are very close to the latter. To overcome this problem, we proceed as follow: we choose an initial guess for ζ_c by solving the following equation that comes from the scaling relations of the envelope provided by Begelman et al. (2008) and Dotan et al. (2011):

$$p_{c,7} = \frac{1.134 (1 - \zeta_c)^{2/5}}{m_\bullet^{16/5} \zeta_c^{28/5}}, \quad (35)$$

where $P_c = p_{c,7} \times 10^7 \text{ erg cm}^{-3}$ and $M_\bullet = m_\bullet M_\odot$. Then, we build a grid of models for several values of ζ_c around the initial guess, and we progressively refine this grid around the solution. When we bracket the true solution with a relative precision $\sim 10^{-3}$, we use this bracketing as the starting points for a Brent root-finder (Brent 1973; Press et al. 2002). The typical solutions of ζ_c are $\lesssim 0.01$; indeed, quasi-stars are radiation-pressure dominated in their interiors. Moreover, we note that ζ typically decreases throughout the radiative layer, reaching values $\zeta \ll 0.01$ at r_{rad} . This behaviour justifies our simplifying assumption of neglecting the gas pressure in the wind, since the ratio $3k_B\rho/(\mu m_p a T^3)$ remains effectively $\ll 1$ through the wind and within the photosphere. Calculations a posteriori of ζ in the wind show a decreasing behaviour. This suggests that our treatment is at least consistent. Of course, the radiation-dominated assumption limits our results to very massive stars and cannot be extended to e.g. Population III stars.

3.3 Results for quasi-stars

We run a grid of models exploring a wide range of M_\bullet and P_c , which maps into M_\star . Fig. 5 summarizes our findings in the M_\bullet – M_\star plane. Specifically, the various panel shows isocontours of the outflow rate \dot{M}_{wind} , the accretion on to the black hole $\dot{M}_{\text{BH}} = L_\bullet/(\eta c^2)$, where the radiative efficiency $\eta \simeq 0.1$, the photospheric luminosity L_{phot} , and the effective, photospheric temperature T_{phot} .

Such a plane is characterized by three regions. For high black hole masses and relatively low envelope masses, no hydrostatic solution can be found (see also Begelman et al. 2008). That is because the quasi-stars would stay beyond the Hayashi (1961) track, which represent a lower limit to the effective temperature (around 4000 K) of a convective envelope in hydrostatic equilibrium. Beyond such a limit, no solutions for the hydrostatic envelope exist. The second region is the evaporation strip identified by Dotan et al. (2011). This region lays where the evaporation time-scale $t_{\text{wind}} = M_\star/\dot{M}_{\text{wind}}$, i.e. the typical time-scale over which the stellar envelope would be blown away by the winds, is shorter than the accretion time-scale $t_\bullet = M_\bullet/\dot{M}_{\text{BH}}$. Within this region, the envelope mass is dispersed by the wind before than the black holes can accrete further. The third region is the growth region, where the black hole can accrete substantial mass from the envelope ($t_\bullet < t_{\text{wind}}$).

We find that the isocontours of \dot{M}_{wind} due to our wind model of Section 2 are different from those in Dotan et al. (2011). Most notably, we do not see any effect of photon-tiring, consistently with our result of Section 2.3 that the ultimate source of the wind kinetic luminosity is the advection luminosity due to internal energy. Specifically, our contours increase mildly when M_\bullet decreases, while they would become suddenly much more steep at the onset of photon-tiring, with \dot{M}_{wind} almost independent of M_\star . At constant M_\bullet , the different shapes of the isocontours are such that \dot{M}_{wind} grows faster at high values of M_\star until it reaches the adiabatic limit discussed in Section 2.3.

When our models hit the adiabatic limit, our quasi-star structures are all characterized by $s_\star = c_{s,\star}^2/v_{\text{esc}}^2$ very close to the value associated with $\mathcal{M}_\star \simeq 0.8$ for an adiabatic wind, as shown by Fig. A1 in the Appendix A. Above this limit, our choice of a specific surface Mach number (≈ 0.8) overconstrains our mathematical system and solutions cannot be found. Technically, we would need to leave \mathcal{M}_\star free to vary and the likely result would be solutions with nearly adiabatic winds.

To test this expectation, we then change method and consider the idealized case of a purely adiabatic wind solution (see Appendix A) and match it to the hydrostatic envelope. These winds are completely specified by the values of the density $\rho(r_{\text{rad}})$ and of the sound speed $c_s(r_{\text{rad}})$ at the end of the envelope. We then check that s associated with $c_s(r_{\text{rad}})$ is in the interval $1/6 < s < 1/4$ in order to have a solution with $\mathcal{M}_\star < 1$ (Fig. A1). Finally, we calculate the adiabatic mass-loss \dot{M}_{ad} according to equation (A7) and we choose the equilibrium solution (i.e. the value of ζ_c) that allows us to match the luminosity L_\bullet to the luminosity carried by the adiabatic wind evaluated at $R_\star = r_{\text{rad}}$, namely $3\dot{M}_{\text{ad}}c_{s,\star}^2(1 + \mathcal{M}_{\text{ad}}^2(c_{s,\star}) - v_{\text{esc}}^2/(6c_{s,\star}^2))$. We find a fairly smooth transition between the two kinds of models, confirming the nearly adiabatic nature of the expected wind when this limit is exceeded (see dashed lines in Fig. 5, top-left panel).

This difference has also the effect of displacing slightly the interface between the evaporation strip and the growth region, i.e. the ‘threshold-growth line’ (Dotan et al. 2011). Our models predict that such a line moves by a factor of ~ 2 – 3 towards higher M_\bullet , decreasing the thickness of the evaporation strip. Moreover, for every point

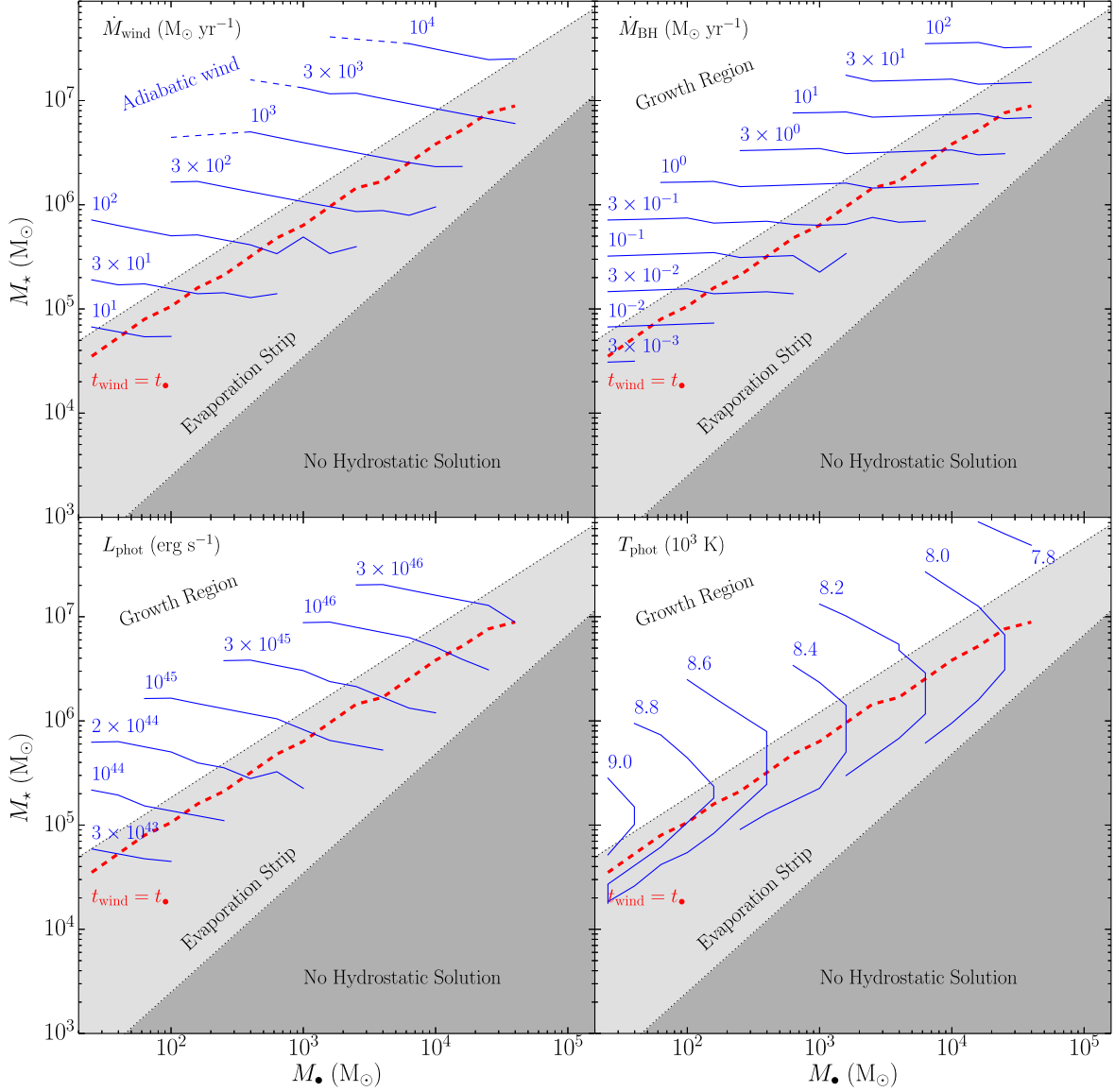


Figure 5. Properties of our quasi-star models in the M_{\bullet} – M_{\star} plane. From upper-left panel, clockwise: thin, blue continuous lines show the isocontours of the outflow rate \dot{M}_{wind} , of the accretion rate on to the black hole \dot{M}_{\bullet} , of the photospheric bolometric luminosity L_{phot} , and of the photospheric effective temperature T_{phot} , respectively. The blue, dashed lines in the upper-left panel show the extension in the adiabatic wind regime of some isocontours as discussed in the text. The adiabatic wind region is labelled explicitly in this panel, while the label ‘Growth Region’ is omitted for clarity. In each panel, the white, light grey and dark grey shaded regions represent the growth region, the evaporation strip (i.e. where $t_{\text{wind}} < t_{\bullet}$), and the region where no hydrostatic solutions exist as reported by Dotan et al. (2011), respectively; on the other hand, the thick, red, dashed line shows the limit of the evaporation strip (i.e. where $t_{\text{wind}} = t_{\bullet}$) for our models.

(M_{\bullet} , M_{\star}) around and within the evaporation strip, we find an \dot{M}_{wind} smaller by a factor $\lesssim 10$ compared to Dotan et al. (2011), which implies a less sudden removal of the envelope when the quasi-star enters the evaporation strip. On the other hand, the isocontours of \dot{M}_{BH} are almost independent of M_{\bullet} and they are similar to previous findings.

The absence of a photon-tired wind has a strong impact on the photospheric luminosity of the quasi-stars. Since the wind is mostly accelerated at the expense of the internal energy, the diffusive luminosity coming out at the photosphere L_{phot} is a large fraction of the luminosity L_{\bullet} originally produced by central accretion and transported through the hydrostatic envelope. Such a luminosity corresponds to Eddington ratios calculated with respect of the whole envelope mass that range from $\Gamma_{\text{phot}} \sim 1$ to $\Gamma_{\text{phot}} \lesssim 10$, even in the

growth region, where Dotan et al. (2011) find a decrease of Γ_{phot} due to photon-tiring. Our models predict photospheric luminosities in the interval $10^{43} \lesssim L_{\text{phot}}/(\text{erg s}^{-1}) \lesssim 10^{47}$, with isocontours similar in shape to those of \dot{M}_{wind} in the M_{\bullet} – M_{\star} plane. Such luminosities are comparable to moderate bolometric luminosities of quasars (e.g. Hopkins, Richards & Hernquist 2007; Mortlock et al. 2011) and might be observable at high redshift as discussed in Section 4 below. At the same time, all our models fall in a narrow range of photospheric temperature between ~ 7500 and ~ 9000 K, with temperatures that decrease approaching the no-hydrostatic-solution region. We recall from Section 2.2 that we define the photosphere as the place where the effective temperature $T_{\text{eff}} \equiv (L/(4\pi r^2 \sigma))^{1/4}$ equals the proxy for the temperature $T \equiv (U/a)^{1/4}$. This happens self-consistently at relatively large optical depth $\bar{\tau} \gtrsim 10$, where T

is physically motivated and correctly influences the optical depth through the opacity law. Moreover, we explicitly check that T_{eff} computed where $\bar{\tau} = 1$ changes by at most ≈ 300 K for all our models, suggesting that our determination of the effective, photospheric temperature T_{phot} is anyway robust. The narrow range of effective temperature is mostly set by the microphysical properties of the gas, specifically by the adopted opacity law. Indeed, the steep temperature dependence of equation (32) is such that the wind becomes optically thin near the opacity drop around $T_0 = 8000$ K. However, the use of the temperature-dependent opacity law (equation 32) in the wind of the quasi-star models does not change significantly the main physical properties of the wind described in Section 2 (i.e. the behaviour of the wind when approaching the adiabatic limit), especially within the photosphere where $\kappa_{\text{eff}}(T) \sim \kappa_{\text{es}}$.

The isocontours of \dot{M}_{wind} , \dot{M}_{BH} (or L_{\bullet}), and L_{phot} behave smoothly enough in the $M_{\bullet}-M_{\star}$ that they can be reasonably well fitted with power laws. By means of a least-square fitting procedure in log-space, we find the following fitting formulas:

$$\dot{M}_{\text{wind}} = (1.4 \pm 0.1) \times 10^{-4} m_{\star}^{0.96} m_{\bullet}^{0.17} M_{\odot} \text{ yr}^{-1}, \quad (36)$$

$$\dot{M}_{\text{BH}} = (8.3 \pm 0.1) \times 10^{-10} m_{\star}^{1.45} m_{\bullet}^{0.03} M_{\odot} \text{ yr}^{-1}, \quad (37)$$

$$L_{\text{phot}} = (3.7 \pm 0.1) \times 10^{38} m_{\star}^{0.94} m_{\bullet}^{0.29} \text{ erg s}^{-1}. \quad (38)$$

These formulas represent the interpolation between the models of our grid. Assuming that quasi-stars evolve through a sequence of equilibrium states (Begelman et al. 2008; Ball et al. 2011; Dotan et al. 2011), we can use them to calculate evolutionary tracks in the $M_{\bullet}-M_{\star}$ plane. We show a few example solutions in Fig. 6, where we assume equations (36) and (37) to be valid also in the adiabatic regime (only relevant for the most massive quasi-star in these examples). Specifically, we solve the equations $\dot{M}_{\star} = \dot{M}_{\text{in}} - \dot{M}_{\text{wind}} - \dot{M}_{\text{BH}}$, and $\dot{M}_{\bullet} = \dot{M}_{\text{BH}}$, where we allow for smooth constant accretion on to the quasi-star envelope through the constant \dot{M}_{in} . When the quasi-star enters the evaporation strip, winds start to become dominant and the envelope mass drops while the black hole cannot grow very efficiently. However, if accretion is intense enough, an almost steady state can be established within the evaporation strip, where the accretion from outside balances the mass-loss due to winds and the black hole can grow until the quasi-stars enters the no-hydrostatic-solution region, which corresponds to a ratio $M_{\star}/M_{\bullet} \lesssim 20$.

4 DETECTABILITY

We have shown that our models of quasi-stars shine with a bolometric photospheric luminosity that is bracketed between $\sim 10^{44}$ and $\sim 10^{46}$ erg s $^{-1}$ for M_{\star} between $\sim 10^5$ and $\sim 10^7 M_{\odot}$. At the same time, we have found that the interval of photospheric temperature is quite narrow around 8500 K. This information allows us to put simple constraints on the detectability of those sources by current and future space-based telescopes such as *HST* and *JWST*, respectively.

Indeed, we can estimate the flux in the filter band X as the magnitude:

$$m_X = M_X + d(z_{\text{source}}) + K_X(z_{\text{source}}), \quad (39)$$

where M_X is the absolute magnitude in band X , $d(z)$ is the distance modulus at the redshift z_{source} of the source, and $K_X(z_{\text{source}})$ is the K -

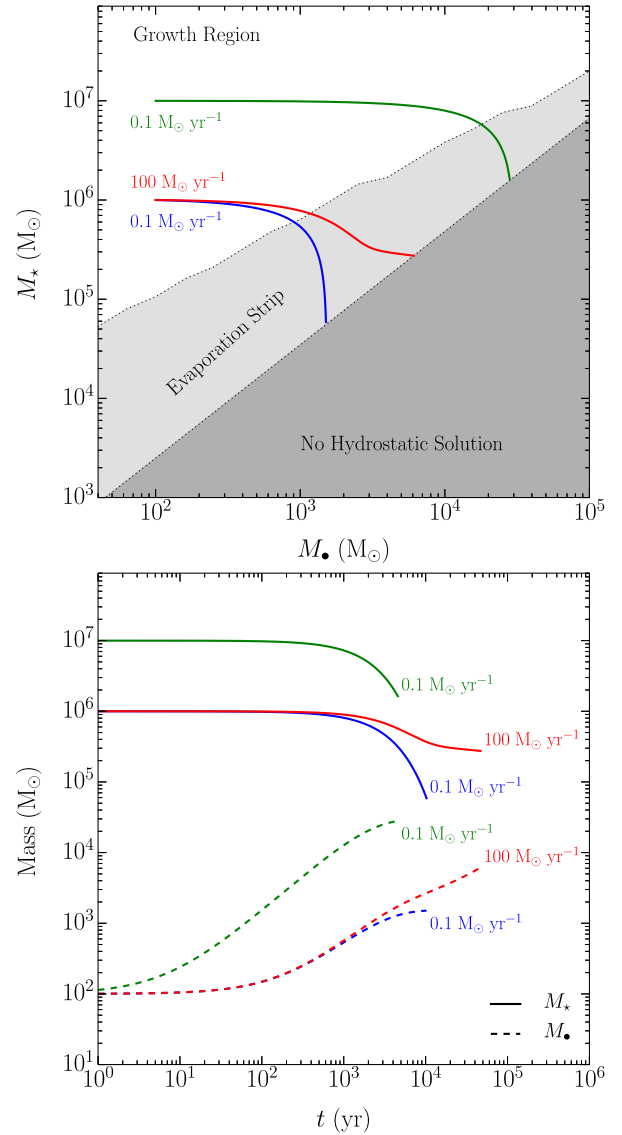


Figure 6. Evolutionary tracks for quasi-stars. Upper panel: evolutionary tracks in the $M_{\bullet}-M_{\star}$ plane (see Fig. 5 for a description, but note that here we plot the evaporation strip determined from our models). The green line corresponds to a quasi-stars with initial $M_{\bullet} = 100 M_{\odot}$, $M_{\star} = 10^7 M_{\odot}$, and $\dot{M}_{\text{in}} = 0.1 M_{\odot} \text{ yr}^{-1}$. The blue and red lines both correspond to a quasi-star with initial $M_{\bullet} = 100 M_{\odot}$, $M_{\star} = 10^6 M_{\odot}$, but with $\dot{M}_{\text{in}} = 0.1 M_{\odot} \text{ yr}^{-1}$ and $\dot{M}_{\text{in}} = 100 M_{\odot} \text{ yr}^{-1}$, respectively. Lower panel: evolution of M_{\bullet} and M_{\star} as a function of time. Continuous and dashed lines (coupled with colours) show the evolution of M_{\star} and M_{\bullet} , respectively.

correction (e.g. Hogg et al. 2002). The distance modulus is defined as

$$d(z) = 25 + 5 \log_{10} \left(\frac{D_L(z)}{\text{Mpc}} \right), \quad (40)$$

and it encapsulates all the dependences on the cosmology through the luminosity distance $D_L(z)$:

$$D_L(z) = (1+z) c H_0^{-1} \int_0^z \frac{dz'}{\sqrt{\Omega_m(1+z')^3 + \Omega_\Lambda}}. \quad (41)$$

Here and in the following we assume the present day values $H_0 = 67.7 \text{ km s}^{-1} \text{ Mpc}^{-1}$, $\Omega_m = 0.309$, and $\Omega_\Lambda = 0.691$ for the Hubble parameter, the matter density, and the density of the cosmological

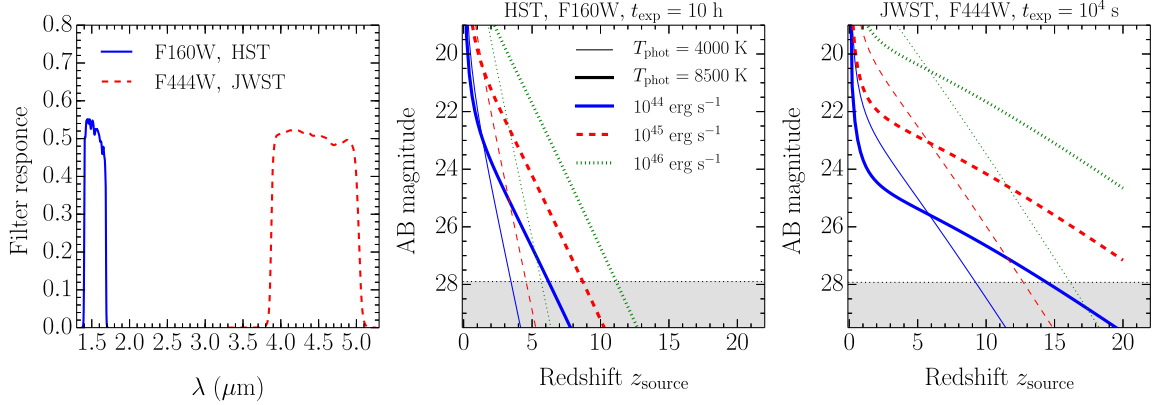


Figure 7. Predictions of the observability of quasi-stars. Left-hand panel: blue, continuous line and red, dashed line show the probability that a photon with wavelength λ is captured by the WFC3 camera+F160W filter mounted on *HST* and by the NIRCcam camera+F444W filter planned for JWST, respectively. Central panel: predicted AB magnitude in the band of the *HST* filter F160W as function of the source redshift z_{source} . Blue-continuous, red-dashed and green-dotted lines refer to the photospheric luminosity $L_{\text{phot}} = 10^{44}, 10^{45}, 10^{46} \text{ erg s}^{-1}$, respectively; thin and thick lines refer to the effective temperature $T_{\text{phot}} = 4000, 8000 \text{ K}$, respectively. Right-hand panel: the same as the central panel, but for the NIRCcam camera+F444W filter planned for JWST.

constant, respectively. These values are consistent with the latest Planck cosmology (Planck Collaboration XIII 2015). The absolute magnitude is the flux as if the source were 10 pc away from the observer:

$$M_X = -2.5 \log_{10} \left[\frac{\int_0^{+\infty} \frac{L_\nu T_X(\nu) \frac{d\nu}{\nu}}{4\pi(10 \text{ pc})^2} \frac{d\nu}{\nu}}{\int_0^{+\infty} g_\nu T_X(\nu) \frac{d\nu}{\nu}} \right], \quad (42)$$

where L_ν is the intrinsic spectral luminosity density (i.e. $L_\nu = dL/d\nu$) of the source, $T_X(\nu)$ is the probability of a photon to get counted at frequency ν with the filter X , and $g_\nu = 3631 \text{ Jy}$ is the constant spectral flux density of a hypothetical reference source used to express magnitudes in the AB system (Oke & Gunn 1983). Following Hogg et al. (2002), we write the K -correction as

$$K_X(z) = -2.5 \log_{10}(1+z) - 2.5 \log_{10} \left[\frac{\int_0^{+\infty} L_\nu T_X \left(\frac{\nu}{1+z} \right) \frac{d\nu}{\nu}}{\int_0^{+\infty} L_\nu T_X(\nu) \frac{d\nu}{\nu}} \right]. \quad (43)$$

The crucial ingredient is the spectra luminosity density L_ν of the source. We assume that L_ν can be modelled as a blackbody at the temperature T_{phot} , emitting the total luminosity L_{phot} . Explicitly, we have

$$L_\nu = \frac{15L_{\text{phot}}}{\pi^4 \nu_{\text{th}}} \frac{(\nu/\nu_{\text{th}})^3}{\exp(\nu/\nu_{\text{th}}) - 1}, \quad (44)$$

where $\nu_{\text{th}} = k_B T_{\text{phot}}/h$ and h is the Planck constant. We discuss the limitations of such an assumption in Section 5.

Having an effective temperature $\sim 8000 \text{ K}$, our quasi-star models are expected to be fairly blue; on the other hand, cosmologically motivated calculations predict that quasi-stars populate mostly massive haloes at $z \gtrsim 10$ (Volonteri & Begelman 2010), with the consequence of displacing the bulk of quasi-star emission in the near-infrared wavelengths $\gtrsim 2 \mu\text{m}$. Therefore, we focus our analysis on the wide filters in the near-infrared at the longest wavelength and contemporary with the highest (effective or predicted) sensibility available for *HST* and JWST. Specifically, we consider the filters

F160W of the Wide Field Camera 3 (WFC3) camera⁵ mounted on *HST* and the filter F444W of the NIRCcam⁶ designed for JWST.

The left-hand panel of Fig. 7 shows the throughput of the considered filters. The *HST* data consider also the coupling between the camera and the filter, while the JWST data are the predicted transmittance of the filter only. In order to mimic the effect of the coupling with the camera for JWST as well, we conservatively multiply the filter transmission by the fudge factor 0.6, obtaining a maximum response similar to the *HST* values ~ 0.5 .

The central and the left-hand panel of Fig. 7 show the predicted flux observed by *HST* and JWST, respectively. We explore the effect of changing the total luminosity of the quasi-star and its effective temperature T_{phot} to compare with Volonteri & Begelman (2010). They assumed an effective temperature of 4000 K, while our fiducial model has 8500 K. We compare two different exposure times for *HST* and JWST, namely $t_{\text{exp}} = 10 \text{ h}$ and $t_{\text{exp}} = 10^4 \text{ s}$, respectively. For comparison, the longest exposure in the F160W band of the *Hubble Ultra Deep Field* '09 captured with the WFC3 camera is $\approx 41 \text{ h}$ ⁷. This choice provides a very similar magnitude limit of ≈ 27.8 for both instruments and filters.

We find that hotter quasi-stars are brighter at higher redshift in the considered bands. This is because at $T_{\text{phot}} = 4000 \text{ K}$, the peak of the spectrum is red enough that at high redshift it gets displaced beyond the band limit of the filters. This happens at $z_{\text{source}} > 3$ for *HST*, while at $z_{\text{source}} > 5-6$ for JWST, because the F444W filter extends more in the near-infrared than the F160W one. Quasi-stars with $L_{\text{phot}} > 10^{45} \text{ erg s}^{-1}$ could be in principle detected by both *HST* and JWST with the considered integration times at $z_{\text{source}} \gtrsim 10$. However, they are close to the magnitude limit for *HST*, while they are well above the same limit for JWST. This suggests that it is fairly unlikely that *HST* has already observed such a source even within a Ultra-Deep-Field-like exposure, whereas we expect JWST to be able to detect quasi-stars in the luminosity range $10^{44}-10^{46} \text{ erg s}^{-1}$ at $z_{\text{source}} > 10$. None the less, as Volonteri & Begelman (2010) have shown, there might be some rare events of quasi-stars forming at redshift as low as $z_{\text{source}} \sim 4$. Though the bulk of the population is

⁵ <http://svo2.cab.inta-csic.es/svo/theory/fps3/>

⁶ <http://www.stsci.edu/jwst/instruments/nircam/instrumentdesign/filters/>

⁷ <https://archive.stsci.edu/prepds/hudf09/>

expected to be in place at higher redshift, *HST* might still observe such an outlier. However, we caution that those numbers represent the most optimistic estimates since we are neglecting the effect of the environment where quasi-stars are expected to live. Indeed, when quasi-stars are harboured within gas-rich environment, part of their radiation might be absorbed and reprocessed in different wavelengths.

5 DISCUSSION AND CONCLUSIONS

Our work addresses the formation of supermassive black hole seeds, a major open issue in galaxy formation and high-energy astrophysics. In particular, we contribute to the assessment of the massive seed scenario from direct collapse of gas at the centre of (proto)galaxies via the quasi-star mechanism. At this stage in time, the assumption that supermassive black holes are grown out of massive seeds formed at redshift > 10 is theoretically and, of course, observationally far from being proved. Whether massive seeds are possible, what is their mass function at birth and the prospect of detectability with future instruments should be critically assessed by a careful investigation of the physical processes at work.

In this context, we focus on the possible super-Eddington growth of embryo black holes inside massive quasi-hydrostatic envelopes (quasi-stars), and we constrain the impact of outflows on to the final mass with which the black hole seed would emerge at the end of this rapid growth phase. This was already addressed in Dotan et al. (2011) but here we consistently solve the full equations for a radiation-dominated wind, including both diffusion and advection of energy in the flow. We find that such winds are ultimately powered by advection luminosity within the flow up to the limit where they become nearly adiabatic (i.e. diffusion luminosity is negligible). When applied to quasi-stars, we find that the final black hole masses are larger but only by a factor of a few with respect to Dotan et al. (2011); in contrast, the observable appearance of quasi-stars is expected to be different. They are luminous (10^{44} – 10^{47} erg s $^{-1}$) blue (effective temperature of ~ 8000 K) objects. In colour, they differ from predictions that ignore mass losses, where temperatures can be up to a factor of 2 lower (Begelman et al. 2008). Their characteristics make them promising targets for JWST, while *HST* may only have detected rare, relative closer ($z < 10$) objects.

Although our wind treatment improves over previous models of quasi-star winds, some caveats need to be discussed. Our steady-state assumption implies that we are not modelling the acceleration region between the hydrostatic envelop and the wind. It is necessary for us to introduce a discontinuity in the physical quantities, and our approach is to assume a vanishingly small acceleration scale, where the velocity jumps from $v \sim 0$ to $\sim 0.8c_s$. In a porous radiation dominated atmosphere, acceleration starts at a radius where inhomogeneities become optically thin on a scale of their size. Since their size is comparable to the density scaleheight, it is also reasonable to assume that significant acceleration happens on that length-scale. In our simulations, we find that the density scaleheight at the onset of the wind is typically 1 per cent of the radius, which supports our simplification of an ‘impulsive’ discontinuity in velocity. Of course, only time-dependent simulations can definitively prove the correctness of this assumption. We also tested the dependence of our models on our working value of $\mathcal{M}_* = 0.8$. As long as $\mathcal{M}_* \gtrsim 0.5$, the main results are weakly sensitive to the exact choice (see also Fig. 2 and Section 2.2.1). However, for lower values of \mathcal{M}_* , solutions can still be found, but show unphysical behaviours when approaching the adiabatic limit. Consistently with the pref-

erence for $\mathcal{M}_* \gtrsim 0.5$ shown in Section 2.2.1, this suggests that a value $\mathcal{M}_* \lesssim 1$ is necessary to better satisfy the assumption of a steady state from the base of the wind.

In contrast with velocity, temperature and density are continuous across the two regions (hydrostatic envelope and wind). This allows us to calculate \dot{M}_{wind} through the continuity equation. We do not adopt the mass-loss rate assumed in Dotan et al. (2011), because it seems to require the presence of a critical point (Shaviv 2001a,b), that is instead absent when solving the equations of a purely radiation dominated wind (equations 1–3). Finally, further progress should include the effect of rotation, which in this version is omitted, and may instead cause larger mass-loss rate around the polar axis. However, a funnel around a polar axis may be carved by the presence of a jet, that would result in a smaller amount of energy being injected into the quasi-star envelope. This last would simply have the effect of changing the black hole mass to envelope mass ratio of a given solution, since for a given quasi-star mass, more accretion energy is needed to support it. More sophisticated 3D simulations, possibly coupling hydrodynamics with radiative transfer, are necessary to validate the overall picture and to assess the impact and interplay of such processes; this opens many possibilities for future additional investigations.

Our assumption of an evolution through equilibria breaks down when the quasi-stars encounter the no-hydrostatic-solution region. Since our approach does not allow us to infer quantitative predictions of the final evolutionary phase, we can only speculate about what might happen afterwards (see also Ball et al. 2011). When a quasi-star reaches this region, the envelope is still a factor of ~ 20 larger than the black hole. Such an envelope cannot remain in hydrostatic equilibrium and it is conceivable that at least a fraction of it may collapse on to the central black hole, leading to further accretion. Since the infalling gas is expected to be radiation-dominated and optically thick, the associated accretion episode might involve a large fraction of mass, at least where the black hole potential dominates (Begelman 1978). This line of reasoning suggests that the masses that we infer in Section 3.3 might be lower limits. However, if the infall proceeds out of equilibrium on a few dynamical time-scales, the inflow rates may be much larger than the Eddington limit of the black hole and feedback may limit further accretion (e.g. Johnson et al. 2011).

Finally, to estimate the detectability of quasi-stars, we assume a blackbody spectrum, that may be accurate for our broad-band luminosity estimates of this pristine object. Of course, reliable spectral predictions must instead account for lines and electron scattering, but this should require a dedicated study (e.g. Schaerer 2002). We also warn the reader that our predictions are for the intrinsic luminosity of quasi-stars and that absorption is not accounted for.

Despite these caveats, our work confirms that super-Eddington accretion on to newly born black holes within quasi-stars is likely responsible for vigorous mass-loss, which in turn may limit the growth of the black holes. If this is the case, forming massive ($> 10^4 M_\odot$) seeds via the quasi-star scenario is therefore more difficult than is generally wished for. It requires massive inflows of gas at the centre ($\geq 10 M_\odot \text{ yr}^{-1}$, see e.g. our Fig. 6), that are generally associated with massive ($> 10^9 M_\odot$) and therefore relative rare haloes at high redshift. This is at least qualitatively in agreement with recent observational studies that fail in finding candidates of massive quasars at $z \gtrsim 5$ and possibly put constraints on the early black hole formation modes (Weigel et al. 2015). To assess how rare those massive seeds are, and whether they can still account for the bright quasars observed at $z > 6$, a consistent cosmological evolution needs to be computed. This is the topic of a follow up paper, that will also allow

us to make a more quantitative assessment of the detectability of these fascinating objects.

ACKNOWLEDGEMENTS

We thank Mitch Begelman, Lucio Mayer, Priyamvada Natarajan, Feryal Özel, Dominik Schleicher, Kevin Schawinski, Mihai Tomozeiu and Marta Volonteri for useful discussions and for a thorough reading of this manuscript in the draft phase. We thank Alan C. Hindmarsh, Carol S. Woodward and the SUNDIALS Team for maintaining the code publicly available. DF is supported by the Swiss National Science Foundation under grant no. 200021_140645.

REFERENCES

- Agarwal B., Dalla Vecchia C., Johnson J. L., Khochfar S., Paardekooper J. P., 2014, *MNRAS*, 443, 648
- Agarwal B., Smith B., Glover S., Natarajan P., Khochfar S., 2015, preprint ([arXiv:1504.04041](https://arxiv.org/abs/1504.04041))
- Agol E., Krolik J., Turner N. J., Stone J. M., 2001, *ApJ*, 558, 543
- Alexander T., Natarajan P., 2014, *Science*, 345, 1330
- Ball W. H., Tout C. A., Żytkow A. N., Eldridge J. J., 2011, *MNRAS*, 414, 2751
- Ball W. H., Tout C. A., Żytkow A. N., 2012, *MNRAS*, 421, 2713
- Baumgarte T. W., Shapiro S. L., 1999, *ApJ*, 526, 941
- Begelman M. C., 1978, *MNRAS*, 184, 53
- Begelman M. C., 1979, *MNRAS*, 187, 237
- Begelman M. C., 2010, *MNRAS*, 402, 673
- Begelman M. C., Shlosman I., 2009, *ApJ*, 702, L5
- Begelman M. C., Volonteri M., Rees M. J., 2006, *MNRAS*, 370, 289
- Begelman M. C., Rossi E. M., Armitage P. J., 2008, *MNRAS*, 387, 1649
- Blandford R. D., Begelman M. C., 2004, *MNRAS*, 349, 68
- Brent R., 1973, *Algorithms for Minimization Without Derivatives*, Dover Books on Mathematics. Dover Publications, New York
- Bromm V., Loeb A., 2003, *ApJ*, 596, 34
- Cassinelli J. P., Castor J. I., 1973, *ApJ*, 179, 189
- Choi J.-H., Shlosman I., Begelman M. C., 2013, *ApJ*, 774, 149
- Choi J.-H., Shlosman I., Begelman M. C., 2015, *MNRAS*, 450, 4411
- Cohen S. D., Hindmarsh A. C., Dubois P. F., 1996, *Comput. Phys.*, 10, 138
- Davies M. B., Miller M. C., Bellovary J. M., 2011, *ApJ*, 740, L42
- Devecchi B., Volonteri M., 2009, *ApJ*, 694, 302
- Devecchi B., Volonteri M., Rossi E. M., Colpi M., Portegies Zwart S., 2012, *MNRAS*, 421, 1465
- Di Matteo T., Khandai N., DeGraf C., Feng Y., Croft R. A. C., Lopez J., Springel V., 2012, *ApJ*, 745, L29
- Dijkstra M., Haiman Z., Mesinger A., Wyithe J. S. B., 2008, *MNRAS*, 391, 1961
- Dijkstra M., Ferrara A., Mesinger A., 2014, *MNRAS*, 442, 2036
- Dotan C., Rossi E. M., Shaviv N. J., 2011, *MNRAS*, 417, 3035
- Fan X. et al., 2006, *AJ*, 131, 1203
- Ferrara A., Loeb A., 2013, *MNRAS*, 431, 2826
- Ferrara A., Salvadori S., Yue B., Schleicher D., 2014, *MNRAS*, 443, 2410
- Ferrarese L., Merritt D., 2000, *ApJ*, 539, L9
- Fowler W. A., 1966, *ApJ*, 144, 180
- Gültekin K. et al., 2009, *ApJ*, 698, 198
- Häring N., Rix H.-W., 2004, *ApJ*, 604, L89
- Hayashi C., 1961, *PASJ*, 13, 450
- Hindmarsh A. C., Brown P. N., Grant K. E., Lee S. L., Serban R., Shumaker D. E., Woodward C. S., 2005, *ACM Trans. Math. Softw.*, 31, 363
- Hogg D. W., Baldry I. K., Blanton M. R., Eisenstein D. J., 2002, ([arXiv:e-prints](https://arxiv.org/abs/0204025))
- Holzer T. E., Axford W. I., 1970, *ARA&A*, 8, 31
- Hopkins P. F., Richards G. T., Hernquist L., 2007, *ApJ*, 654, 731
- Hosokawa T., Omukai K., Yorke H. W., 2012, *ApJ*, 756, 93
- Hosokawa T., Yorke H. W., Inayoshi K., Omukai K., Yoshida N., 2013, *ApJ*, 778, 178
- Igumenshchev I. V., Abramowicz M. A., 1999, *MNRAS*, 303, 309
- Johnson J. L., Bromm V., 2007, *MNRAS*, 374, 1557
- Johnson J. L., Khochfar S., Greif T. H., Durier F., 2011, *MNRAS*, 410, 919
- Kato M., 1983, *PASJ*, 35, 33
- Latif M. A., Schleicher D. R. G., Schmidt W., Niemeyer J., 2013, *MNRAS*, 433, 1607
- Lodato G., Natarajan P., 2006, *MNRAS*, 371, 1813
- Lupi A., Colpi M., Devecchi B., Galanti G., Volonteri M., 2014, *MNRAS*, 442, 3616
- McConnell N. J., Ma C.-P., 2013, *ApJ*, 764, 184
- Madau P., Rees M. J., 2001, *ApJ*, 551, L27
- Madau P., Haardt F., Dotti M., 2014, *ApJ*, 784, L38
- Magorrian J. et al., 1998, *AJ*, 115, 2285
- Marconi A., Hunt L. K., 2003, *ApJ*, 589, L21
- Mayer M., Duschl W. J., 2005, *MNRAS*, 358, 614
- Mayer L., Kazantzidis S., Escala A., Callegari S., 2010, *Nature*, 466, 1082
- Mayer L., Fiacconi D., Bonoli S., Quinn T., Roškar R., Shen S., Wadsley J., 2015, *ApJ*, 810, 51
- Milosavljević M., Bromm V., Couch S. M., Oh S. P., 2009, *ApJ*, 698, 766
- Mortlock D. J. et al., 2011, *Nature*, 474, 616
- Oke J. B., Gunn J. E., 1983, *ApJ*, 266, 713
- Owocki S. P., Gayley K. G., Shaviv N. J., 2004, *ApJ*, 616, 525
- Pelupessy F. I., Di Matteo T., Ciardi B., 2007, *ApJ*, 665, 107
- Planck Collaboration XIII 2015, preprint ([arXiv:1502.01589](https://arxiv.org/abs/1502.01589))
- Press W. H., Teukolsky S. A., Vetterling W. T., Flannery B. P., 2002, *Numerical Recipes in C++ : The Art of Scientific Computing*. Cambridge Univ. Press, Cambridge
- Quataert E., Gruzinov A., 2000, *ApJ*, 539, 809
- Quinlan G. D., Shapiro S. L., 1990, *ApJ*, 356, 483
- Quinn T., Paczynski B., 1985, *ApJ*, 289, 634
- Schaerer D., 2002, *A&A*, 382, 28
- Shaviv N. J., 2001a, *MNRAS*, 326, 126
- Shaviv N. J., 2001b, *ApJ*, 549, 1093
- Shibata M., Shapiro S. L., 2002, *ApJ*, 572, L39
- Stone J. M., Pringle J. E., Begelman M. C., 1999, *MNRAS*, 310, 1002
- Tanaka T., Haiman Z., 2009, *ApJ*, 696, 1798
- Treister E., Schawinski K., Volonteri M., Natarajan P., 2013, *ApJ*, 778, 130
- Tremaine S. et al., 2002, *ApJ*, 574, 740
- Volonteri M., Begelman M. C., 2010, *MNRAS*, 409, 1022
- Volonteri M., Haardt F., Madau P., 2003, *ApJ*, 582, 559
- Volonteri M., Silk J., Dubus G., 2015, *ApJ*, 804, 148
- Weigel A. K., Schawinski K., Treister E., Urry C. M., Koss M., Trakhtenbrot B., 2015, *MNRAS*, 448, 3167
- Żytkow A., 1972, *Acta Astron.*, 22, 103

APPENDIX A: REVIEW OF ADIABATIC WINDS

For convenience, we briefly review the main features of an adiabatic wind characterized by the equation of state $p = K\rho^{4/3}$, where K is a constant (for further and more general readings, see e.g. Holzer & Axford 1970). Within the formalism introduced in Section 2.1, the equations of such an isentropic wind are

$$\left(1 - \frac{s}{w}\right) w' = -1 + \frac{4s}{1-x}, \quad (\text{A1})$$

$$w' + 6s' + 1 = 0. \quad (\text{A2})$$

These equations can be derived by our starting equations of Section 2.1 in the optically thick limit when $\kappa \rightarrow +\infty$ and $L(r) \rightarrow 0$. From the equation above, we immediately see that the critical (or sonic) point (i.e. where $w = s$), when present, coincides with the singular point where w' can diverge. To avoid that, we require that the left-hand side of equation (A1) is 0 at the critical point x_c , which implies the relation between x_c and the critical velocity w_c

$$x_c = 1 - 4w_c. \quad (\text{A3})$$

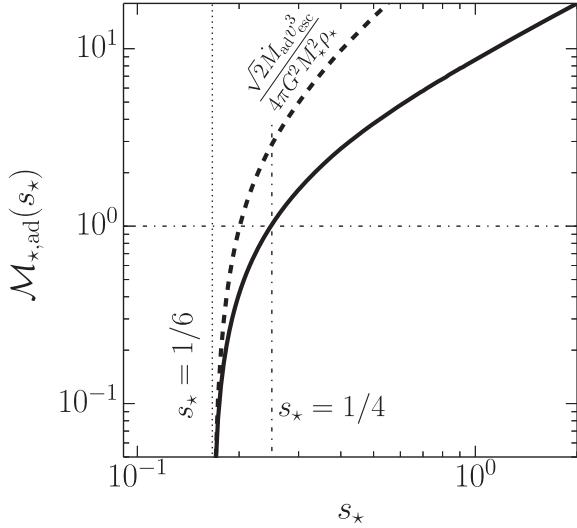


Figure A1. Relation $\mathcal{M}_{*,ad}(s_*)$ between the sound speed and the Mach number at R_* for an adiabatic wind (thick continuous line). The thick, dashed line shows the scaling of the mass outflow rate \dot{M}_{ad} with the sound speed $c_{s,*}$. The thin, dotted line shows the position $s_* = 1/6$, where the Mach number approaches asymptotically zero. The thin, dot-dashed lines show that when $s_* = 1/4$, the wind has $\mathcal{M}_* = 1$ exactly at R_* .

This equation shows that the maximum speed w_c to have a critical point outside the stellar surface (i.e. $x_c \geq 0$, which corresponds to a subsonic solution at R_*) is $w_c \leq 1/4$, or $v_c^2 \leq GM_*/(2R_*)$. On the other hand, a critical point approaching infinity (i.e. $x_c \rightarrow 1$) corresponds to a critical velocity $w_c \rightarrow 0$.

Equation (A2) describes the conservation of energy and entropy. The request of a non-diverging critical point sets the total energy associated with wind:

$$e \equiv w + 6s + x = 3w_c + 1. \quad (\text{A4})$$

This condition, when evaluated at R_* , provides a relation between w_c and the quantities w_* and s_* . The second condition that allows

a full determination of w_* and s_* given w_c is the conservation of mass, which reads as equation (1), combined with the relation $\rho/\rho_* = (s/s_*)^3$, which comes from the equation of state and the general definition of sound speed in equation (25). The final and complete relations between w_c and w_* and s_* are

$$w_* + 6s_* = 3w_c + 1, \quad (\text{A5})$$

$$16 w_*^{1/2} s_*^3 = w_c^{3/2}. \quad (\text{A6})$$

When $w_c \rightarrow 0$, the second relation shows that $w_*^{1/2} s_*^3 \rightarrow 0$ and either w_* or s_* has to go to zero. Since this limit case corresponds to have a critical point well outside R_* , we have $w_* \ll s_*$ and therefore $w_* \rightarrow 0$. The first relation then imply that every adiabatic solution with a critical point at a finite radius has necessarily $s_* > 1/6$, while every solution with a critical point at a finite radius larger than R_* requires $1/6 < s_* < 1/4$. Combining equations (A5) and (A6) provides also a unique relation $\mathcal{M}_{*,ad}(s_*)$ between the sound speed and the Mach number at R_* . This relation is shown in Fig. A1.

We can finally estimate the mass outflow rate through the conditions at the critical point and map them back to the properties of the flow at R_* . At the critical point, the outflow rate reads $\dot{M} = 4\pi r_c^2 \rho(r_c) v_c$. Using the relations $r_c = GM_*/(2v_c^2)$, $\rho(r_c) = \rho_*(v_c/c_{s,*})^6$ and equation (A5) in dimensional form, we obtain

$$\dot{M}_{ad} = \frac{4\pi G^2 M_*^2 \rho_*}{\sqrt{2} c_{s,*}^3} \left(1 + \frac{\mathcal{M}_{*,ad}^2(c_{s,*})}{6} - \frac{v_{esc}^2}{6c_{s,*}^2} \right)^{3/2}. \quad (\text{A7})$$

This depends on the properties of the star, such as M_* and v_{esc} , on the density ρ_* that sets the normalization, and on the sound speed $c_{s,*}$. Fig. A1 shows also the scaling of \dot{M}_{ad} with the sound speed $c_{s,*}$.

This paper has been typeset from a $\text{\TeX}/\text{\LaTeX}$ file prepared by the author.